

# Redox Modulator Iron Complexes Trigger Intrinsic Apoptosis Pathway in Cancer Cells

## Introduction

Cancer is the leading source of deaths worldwide and the emergence of drug resistance to the existing class of anticancer therapeutics warrants novel therapeutic interventions. While organic small molecule therapeutics continue to dominate the medicinal chemistry, milestone therapeutic, cisplatin is crowned as the major metal-based therapeutic to rule cancer therapy for the past four decades.<sup>1</sup> Apart from cisplatin,<sup>1</sup> carboplatin and oxaliplatin are the follow-up platinum drugs widely used for treating cancer and these molecules predominantly function through the platination of DNA (deoxyribonucleic acid) by intrastrand cross-linking of deoxyguanosine residues in cells amongst several other mechanisms.<sup>2</sup> Metal-based therapeutics that operate beyond DNA targeting mechanisms in cancer cells could serve as potential alternatives to strengthen the arsenal of metal-based anticancer drugs.<sup>3-12</sup> Metal ion homeostasis is essential for cell signaling, growth, survival, and metabolism.<sup>13</sup> Particularly, systemic functions and metabolism of iron are regulated by ferroportin and iron-regulatory proteins.<sup>13</sup> Transferrin, iron-responsive element-binding proteins (IRPs), and iron-sulfur cluster proteins (ISCs) transfer and regulate iron homeostasis in cells, which are critical for oxygen transport, respiration, cell signaling, proliferation, and metabolism.<sup>14</sup> However, the accumulation of free iron and disruption of its homeostasis is recorded in several cancers and other diseases.<sup>13,15,16</sup> The ROS-generating capability of free iron pools leading to DNA damage and mutations are well characterized as responsible factors for cancer onset and progression.<sup>17</sup> In parallel, a high level of iron is essential for balancing the fast metabolism and respiration in cancer cells, for example, bone and liver cancer cells are known to possess high iron content than their respective normal cells.<sup>17-20</sup> Trapping intracellular metal ions using organic ligands has proved successful in eliminating the tumor.<sup>21-23</sup> Oxidative phosphorylation in mitochondria and glycolysis for energy production are predominant in cancer cells even under aerobic conditions ('Warburg effect').<sup>24</sup> Therefore, a disruption of this oxidative metabolism by depleting intracellular iron would make the cancer cells sensitive to treatment. We hypothesized to additionally challenge the cancer cell survival by turning its intracellular iron into an iron complex capable of generating deleterious ROS that could promote oxidative cell death. Here we report the identification of iron complexes and their ligands, a nitrogen-based heterocyclic scaffolds chelating with iron, that oxidatively impair mitochondrial function to trigger intrinsic apoptosis pathway in cancer cells

## Objectives

- Designing and development of ligand molecules that forms complex with Iron
- Elucidation of efficacy of developed ligands and complexes against cancer cell lines

- Identification of mode of action of molecules in the prevention of proliferation of cancer cells
- Development of nano encapsulated ligands and complexes for betterment of anti-proliferative efficiency in the cancer cells

## Materials and methods

### 1. Chemistry methods:

#### General methods for synthesis and characterization:

All chemicals and reagents were obtained from commercial sources and were used as received. HPLC grade solvents, H<sub>2</sub>O and CH<sub>3</sub>CN from Merck were used in spectroscopic studies. Elemental analyses (C, H, N) were obtained using Perkin Elmer CHNS/O 2400 series II Analyser. IR spectrum was recorded using Zn-Se pellets with an ECO-ATR spectrometer (Bruker Alpha II). Agilent 8453 diode-array spectrophotometer was used to record UV/Vis absorption spectra and conduct kinetic experiments spectrophotometrically in 1 cm quartz cells ( $\lambda$  = 190 – 1100 nm range). The Bruker EMX 1444 spectrometer with the temperature controller was employed to record the X-band EPR data at 120 K. Simulation of EPR spectrums was carried out by Bruker WINEPR SimFonia software. The spectrometer was calibrated using 3-bwasdiphenylene-2-phenylallyl (BDPA) as X-Band EPR standard.

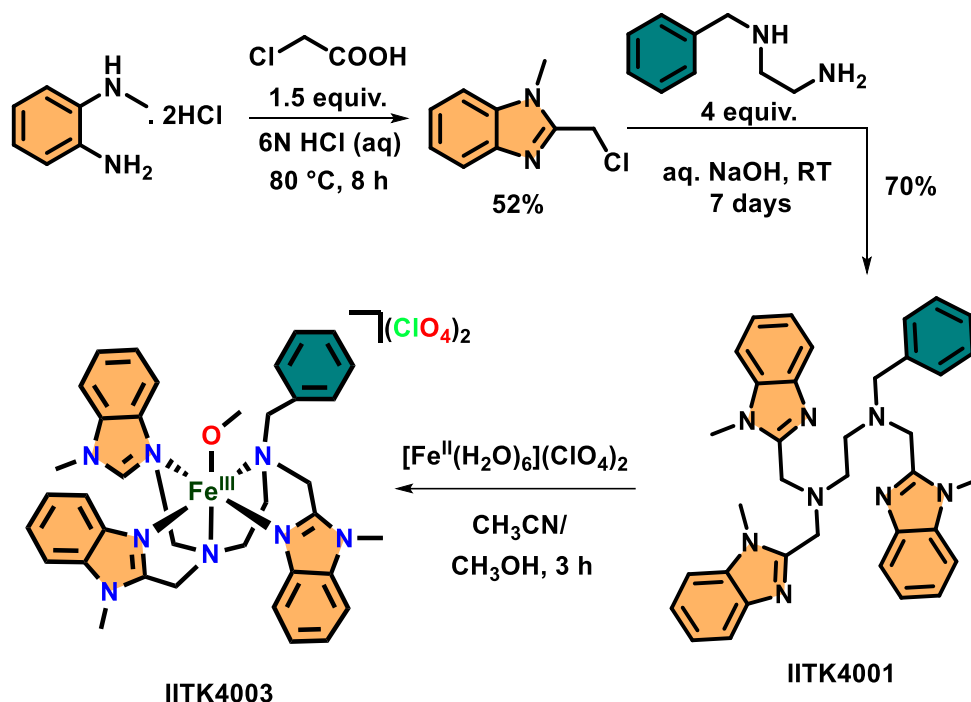
Cyclic Voltammetry experiments were carried out at room temperature using the CH instruments Electrochemical Analyzer M-600B series. A three-electrode system was used where glassy carbon was used as a working electrode, Pt wire as an auxiliary electrode, and the aqueous Ag/AgCl the reference electrode. The solutions used were 1 mM of complex and 120 mM of supporting electrolyte tetra-n-butylammonium perchlorate in acetonitrile and potassium nitrate in water, respectively.

**X-ray crystallography:** Single-crystal of suitable dimensions was used for data collection. Diffraction intensities were collected on a Bruker APEX-II CCD diffractometer, with graphite-monochromated Mo K $\alpha$  (0.71073 Å) radiation at 100(2) K. Data were corrected for Lorentz and polarization effects; empirical absorption corrections (SADABS v 2.10) were applied. Using Olex2,<sup>7</sup> the structures were solved by ShelXT<sup>8</sup> structure solution program using Intrinsic Phasing and refined with the ShelXL<sup>9</sup> refinement package using Least Squares minimization. The position of the hydrogen atoms was calculated by assuming ideal geometries but not refined. All non-hydrogen atoms were refined with anisotropic thermal parameters by full-matrix least-squares procedures on F<sup>2</sup>. **CCDC 2206145, and 2206291** contain the supplementary crystallographic data for IITK4004, and IITK4007 respectively. This data can be obtained free of charge from the Cambridge Crystallographic Data Centre via [www.ccdc.cam.ac.uk](http://www.ccdc.cam.ac.uk).

#### 1.1 Synthesis and characterization:

**Synthesis of 2-(chloromethyl)-1-methyl-1H-benzo[d]imidazole:** N-methylbenzene-1,2-diamine (3 g, 15.4 mmol) was dissolved in 32 mL of 6 N HCl followed by the addition of 2-chloroacetic acid (2.168 g, 23.07 mmol) in a round-bottom flask. The reaction was refluxed at 80 °C for 8 hours. The reaction was cooled down to room temperature, followed by

addition of an aqueous ammonia solution dropwise to neutralize the excess acid in an ice bath with continuous stirring.



#### Scheme S1. Synthesis of IITK4001 and IITK4003:

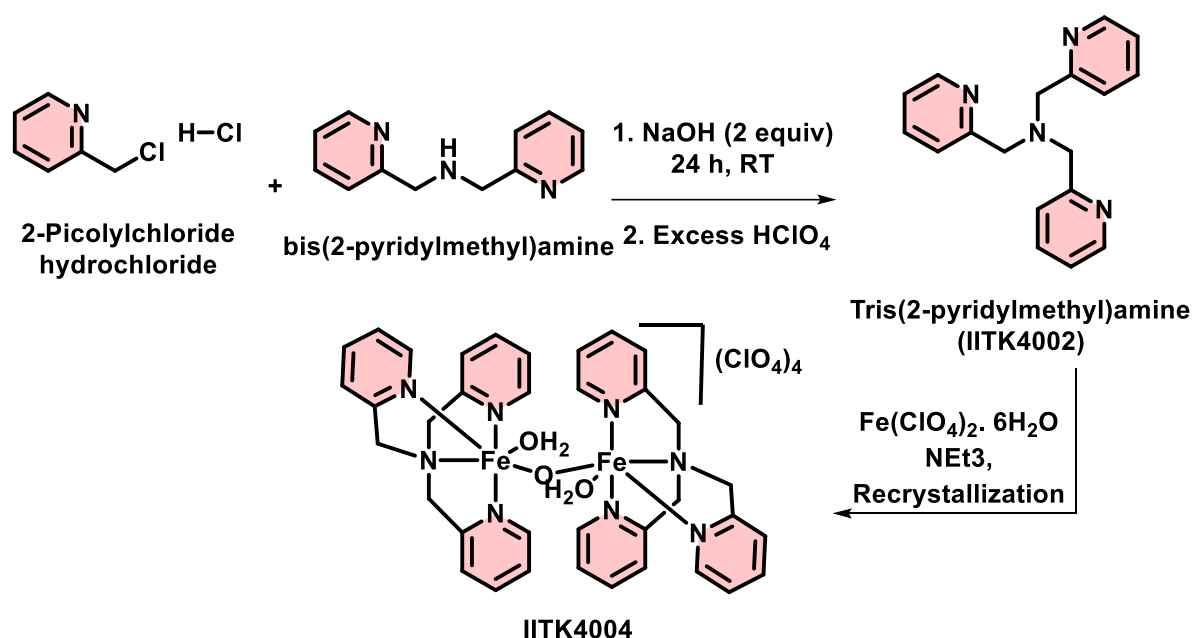
Brown precipitate appeared after neutralisation that was filtered over G2 frit and washed with cold water. The solid was kept for drying overnight in a vacuum desiccator. The crude was purified by column chromatography over neutral alumina, using chloroform as eluting solvent. The crude obtained after column, redissolved in  $\text{CHCl}_3$  and excess hexane poured in it. The slow evaporation of the solution gives white crystals of product within 2 days. Yield: 1.47 g, 52 %.  $^1\text{H}$  NMR (400 MHz,  $\text{CDCl}_3$ ):  $\delta$  (ppm) 7.76 – 7.75 (d, 1H,  $J = 7.44$  Hz), 7.35 – 7.27 (m, 3H), 4.83 (s, 2H), 3.84 (s, 3H).  $^{13}\text{C}$  NMR ( $\text{CDCl}_3$ , 100 MHz):  $\delta$  (ppm) 149.10, 142.05, 136.23, 123.75, 122.80, 120.23, 109.61, 36.90, 30.34.

**Synthesis of  $\text{N}^1$ -benzyl- $\text{N}^1, \text{N}^2, \text{N}^2$ -tris((1-methyl-1H-benzo[d]imidazol-2-yl)methyl)ethane-1,2-diamine (IITK4001):** 2-(chloromethyl)-1-methyl-1H-benzo[d]imidazole (1.5 g, 8.33 mmol) was dissolved in 15 mL of water followed by  $\text{N}^1$ -benzylethane-1,2-diamine (424.3  $\mu\text{L}$ , 2.7 mmol) in a round-bottom flask equipped with a stir bar. Aqueous NaOH solution (0.33 g, 8.33 mmol) was slowly added dropwise over a period of an hour. The resulting mixture was stirred at room temperature for 7 days. The reaction mixture was extracted three times with 25 mL of methylene chloride. The combined organic phases were dried over  $\text{Na}_2\text{SO}_4$ , and the solvent was evaporated under reduced pressure. Yield: 1 g (70 %). Characterization:  $^1\text{H}$  NMR (400 MHz,  $\text{CDCl}_3$ )  $\delta$  (ppm) 7.70 – 7.66 (m, 3H), 7.24 – 7.22 (m, 6H), 7.16 (d, 2H,  $J = 4$  Hz), 7.16 – 7.14 (m, 2H), 7.13 (d, 4H,  $J = 1.44$  Hz), 3.90 (s, 4H), 3.79 (s, 2H), 3.58 (s, 2H), 3.44 (s, 3H), 3.36 (s, 6H), 2.89 (t, 2H,  $J = 6.28$  Hz), 2.73 (t, 2H,  $J = 6.32$  Hz).  $^{13}\text{C}$  NMR (100 MHz,  $\text{CDCl}_3$ )  $\delta$  (ppm) 151.64, 151.17, 135.93, 129.39, 128.35, 127.47, 122.97, 122.34, 118.56, 119.25, 109.42, 109.33, 59.61, 52.62, 51.76, 51.49, 51.35, 30.00, 29.68.

**Synthesis of  $[\text{Fe}^{\text{III}}(\text{BnTBEN})(\text{OCH}_3)](\text{ClO}_4)_2$  (IITK4003):** In a round-bottom flask  $[\text{Fe}^{\text{II}}(\text{H}_2\text{O})_6](\text{ClO}_4)_2$  (62.28 mg, 0.171 mmol) was dissolved in the minimum amount of acetonitrile. To this equimolar amount of BnTBEN (100 mg, 0.171 mmol) solution in  $\text{CH}_3\text{OH}$  was added dropwise. Reaction stirred for 3 h at room temperature. Excess diethyl ether poured in the reaction mixture to get red precipitate, washed thrice with diethyl ether. This precipitate dried under vacuum. Yield: 110 mg (70.9 %). Single crystals suitable for X-ray analysis were obtained by the slow vapour diffusion of diethyl ether into the 1:1 acetonitrile: $\text{CH}_3\text{OH}$  solution of IITK4003 at room temperature. UV Vis: 245nm ( $\varepsilon = 42480 \text{ M}^{-1} \text{ cm}^{-1}$ ), 272 nm ( $\varepsilon = 52800 \text{ M}^{-1} \text{ cm}^{-1}$ ), 280nm ( $\varepsilon = 50400 \text{ M}^{-1} \text{ cm}^{-1}$ ) and a broad band at 376 nm ( $\varepsilon = 8400 \text{ M}^{-1} \text{ cm}^{-1}$ ). Anal. Calc. for  $\text{C}_{37}\text{H}_{41}\text{Cl}_2\text{FeN}_8\text{O}_9$ : C 51.17, H 4.76, N 12.90. Found: C 51.59, H 4.78, N 13.37.

**Synthesis, Characterization and reactivity of  $[\text{Fe}^{\text{III}}_2(\text{TPA})_2(\mu\text{-O})(\text{H}_2\text{O})_2](\text{ClO}_4)_4$  IITK4004**

**Scheme S2. Synthesis of IITK4002 and IITK4004:**



**Synthesis of tris(2-pyridylmethyl)amine (TPA, IITK4002):** The ligand tris(pyridin-2-ylmethyl)amine (TPA) was synthesized as per literature reports and the characterization data were in agreement with the reported ones.<sup>10</sup>

**Synthesis of  $[\text{Fe}^{\text{III}}_2(\text{TPA})_2(\mu\text{-O})(\text{H}_2\text{O})_2](\text{ClO}_4)_4$  (IITK4004):** A red coloured solution was obtained by combining 2 mL acetonitrile solution of  $[\text{Fe}^{\text{II}}(\text{H}_2\text{O})_6](\text{ClO}_4)_2$  (199 mg, 0.55 mmol) to 2 mL acetonitrile solution of IITK4002 (159.5 mg, 0.55 mmol) at room temperature. After stirring the reaction mixture for three hours, half of the volume was removed under reduced pressure. Upon adding excess diethyl ether to the reaction mixture, a red-coloured precipitate was obtained. The precipitate of IITK4004 was washed with diethyl ether (3 x 25 mL) and dried under reduced pressure. Crystallization was accomplished through diethyl ether vapour diffusion into an acetonitrile solution of IITK4004. Red-coloured shiny needle-like crystals suitable for X-ray analyses were obtained in 2 days at 25 °C. Yield: 150 mg (24%).

Elemental Analysis: Calculated for  $[\text{Fe}^{\text{III}}_2(\text{TPA})_2(\mu\text{-O})(\text{H}_2\text{O})_2](\text{ClO}_4)_4$ : C 37.85%, H 3.53%, N 9.78%. Found, C 37.11%, H 3.36%, N 9.52%.

**Synthesis of  $[\text{Zn}^{\text{II}}(\text{TPA})(\text{H}_2\text{O})](\text{CF}_3\text{SO}_3)_2$  (IITK4007):** To a 2 mL of  $\text{CH}_3\text{CN}$  solution containing IITK4002 (50.5 mg, 174  $\mu\text{mol}$ ), 4 mL  $\text{CH}_3\text{CN}$  solution of  $[\text{Zn}^{\text{II}}(\text{H}_2\text{O})_6](\text{CF}_3\text{SO}_3)_2$  (63.2 mg, 174  $\mu\text{mol}$ ) was added at room temperature. After stirring for 3 h, the solvent was removed in vacuo to produce IITK4007 as a white solid. Then, the recrystallization of IITK4007 carried out through diethyl ether vapour diffusion into acetonitrile solution at room temperature afforded white crystals of  $[\text{Zn}^{\text{II}}(\text{TPA})(\text{H}_2\text{O})](\text{CF}_3\text{SO}_3)_2$  complex suitable for X-ray analyses. Yield: 72 mg (62%).

**UV-Vis studies of *in situ* prepared  $[\text{Fe}^{\text{II}}(\text{BnTBEN})(\text{NCCH}_3)](\text{ClO}_4)_2$  (at  $-40^\circ\text{C}$ ):** Stock solution of  $[\text{Fe}^{\text{II}}(\text{H}_2\text{O})_6](\text{ClO}_4)_2$  was prepared in acetonitrile and BnTBEN in dichloromethane (DCM). While performing the UV Vis kinetic studies  $[\text{Fe}^{\text{II}}(\text{H}_2\text{O})_6](\text{ClO}_4)_2$  was added at room temperature in cuvette and ligand at  $-40^\circ\text{C}$ . After stirring for a few seconds, bands at 285 nm ( $\varepsilon=10250\text{ M}^{-1}\text{ cm}^{-1}$ ) and 272 nm ( $\varepsilon=11000\text{ M}^{-1}\text{ cm}^{-1}$ ) were observed. (Fig S35)

**Generation of Fe (IV) oxo species using mCPBA:** The treatment of *in situ* generated  $[\text{Fe}^{\text{II}}(\text{BnTBEN})(\text{NCCH}_3)](\text{ClO}_4)_2$  with 1 equivalent of mCPBA in acetonitrile at  $-40^\circ\text{C}$  leads to the formation of a stable band at 775 nm (within 20 sec.) which is a characteristic band for high valent Iron(IV)oxo species. (Fig. S38)

## 2. Biology: Materials and Methods:

### Statistics and reproducibility:

Data were expressed as mean  $\pm$  s.d. and P values were calculated using an unpaired two-tailed Student's t-test for pairwise comparison of variables with a 95% confidence interval and  $n - 2$  degrees of freedom, where  $n$  is the total number of samples, in all Figures. Each of the biological studies were performed in two independent cell lines (Huh-7 and U2OS) and are representative of two or more independent experiments with a minimum of triple technical replicates.

**Cell culture:** U2OS, Huh-7, H9C2, A375, U87MG, HCT116, HEK293 were grown in DMEM (Dulbecco's Modified Eagle Medium Gibco). A549, PC-3, MDA-MB-231, MCF-7, RPMI8226, Jurkat-J6 cell lines were grown in RPMI 1640. DMEM and RPMI media were supplemented with 10% FBS (Foetal Bovine Serum- Gibco) and 1% PenStrep (Pencillin Streptomycin- Gibco)

### Cell viability screening of the ligand library against U2OS cells using CellTiter-Glo assay:

Cells were cultured in T75 flasks (Thermo) until they attain 70%-80% confluency. Cells were trypsinized with 4 mL of trypsin (0.25% Trypsin-EDTA - Gibco) and counted by using a hemocytometer. In 384 well plate, 500 cells/well with 75  $\mu\text{L}$  media were plated into 360 wells (Thermo). The remaining 24 wells were plated with only media. Plates were incubated at  $37^\circ\text{C}$ , 5%  $\text{CO}_2$  (Forma steri cycle  $\text{CO}_2$  incubator - Thermo Fisher Scientific) for 24 hours. Cells were treated with 20  $\mu\text{M}$  and 5  $\mu\text{M}$  ligands in triplicate. 0.1% DMSO (SRL) was used as negative control, 533 nM doxorubicin (sigma) and 5  $\mu\text{M}$  of cisplatin (Alfa-Aesar) were used as positive controls. Cells were incubated for 72 hours at  $37^\circ\text{C}$ , 5%  $\text{CO}_2$  after treatment. After 72 hours of incubation cell viability was measured using CellTiter-Glo assay (Promega). Briefly, media was discarded from the wells and 30  $\mu\text{L}$  of 1X CellTiter-Glo diluted in 1X PBS

was added to all the wells in dark conditions and incubated at room temperature for 5 minutes. The 384 well plate was centrifuged (Thermo Fisher Scientific) for 1 minute at 1000 RPM and luminescence readings were recorded in multimode plate reader (GloMax Explorer - Promega). Percentage cell viability was calculated as  $((\text{luminescence of treated cells} - \text{luminescence of media control}) / (\text{luminescence of DMSO controls} - \text{luminescence of media control})) * 100$ . Bar graphs were plotted by using the Graphpad Prism 9.0 software. The data provided are representative of three or four independent experiments.

**Dose-dependent cell viability studies in cancer cells by CellTiter-Glo assay:** U2OS, Huh-7 cells were cultured and processed as discussed above. Then, the plated cells in a 384-well plate were treated with 8 different concentrations of various compounds in triplicate as follows. The concentrations of IITK4001 and IITK4002 are 10  $\mu\text{M}$ , 3.33  $\mu\text{M}$ , 1.11  $\mu\text{M}$ , 0.37  $\mu\text{M}$ , 0.123  $\mu\text{M}$ , 0.0411  $\mu\text{M}$ , 0.0137  $\mu\text{M}$ , 0.0045  $\mu\text{M}$ . Concentrations of IITK4004, IITK4005, IITK4007, IITK4006 are - 100  $\mu\text{M}$ , 33.3  $\mu\text{M}$ , 11.1  $\mu\text{M}$ , 3.7  $\mu\text{M}$ , 1.23  $\mu\text{M}$ , 0.411  $\mu\text{M}$ , 0.137  $\mu\text{M}$ , 0.045  $\mu\text{M}$ ; IITK4005, IITK4006, IITK4007, Ferrostatin (AK Scientific), Deferoxamine mesylate (GLR Innovations),  $\text{H}_2\text{O}_2$  (TCI), *t-BuOOH* (GLR), staurosporine (sigma) - 100  $\mu\text{M}$ , 33.3  $\mu\text{M}$ , 11.1  $\mu\text{M}$ , 3.7  $\mu\text{M}$ , 1.23  $\mu\text{M}$ , 0.411  $\mu\text{M}$ , 0.137  $\mu\text{M}$ , 0.045  $\mu\text{M}$ ; sodium azide - 20 mM, 6.66 mM, 2.22 mM, 0.74 mM, 0.24 mM, 0.08 mM, 0.027 mM, 0.009 mM. 0.1% DMSO was used as negative control, 0.5 mM doxorubicin and 5  $\mu\text{M}$  of cisplatin positive control conditions were used in the treatment. Cells were incubated for 72 hours at 37  $^{\circ}\text{C}$ , 5%  $\text{CO}_2$  after treatment. After 72 hours of incubation, media was discarded from the wells and 30  $\mu\text{L}$  of 1X CellTiter-Glo diluted in 1X PBS was added to all the wells in dark conditions and incubated at room temperature for 5 minutes. The 384 well plate was centrifuged for 1 minute at 1000 RPM and luminescence readings were recorded in multimode plate reader. Percentage cell viability was calculated as  $((\text{luminescence of treated cells} - \text{luminescence of media control}) / (\text{luminescence of DMSO controls} - \text{luminescence of media control})) * 100$ . Graphs were plotted by using non-linear regression curve fit programme of Graphpad Prism 9.0.  $\text{EC}_{50}$  was calculated using Graphpad Prism software. The data provided are representative of three or four independent experiments.

**Dose-dependent cell viability studies in U2OS cell line by Resazurin assay:** Cells were cultured and processed as discussed above. Cells were treated with 8 different concentrations of Ferrostatin, Deferoxamine mesylate, RSL-3 (Adooq Biosciences), QVD-OPH (Adooq Biosciences) in triplicate. Concentrations of compounds were as follows, 100  $\mu\text{M}$ , 33.3  $\mu\text{M}$ , 11.1  $\mu\text{M}$ , 3.7  $\mu\text{M}$ , 1.23  $\mu\text{M}$ , 0.411  $\mu\text{M}$ , 0.137  $\mu\text{M}$ , 0.045  $\mu\text{M}$ ; 0.1% DMSO was used as negative control, 533 nM doxorubicin and 5  $\mu\text{M}$  of cisplatin positive control conditions were used in the treatment. Cells were incubated for 72 hours at 37  $^{\circ}\text{C}$ , 5%  $\text{CO}_2$  after treatment. After 72 hours of incubation, media was discarded from the wells and washed with 1X PBS. 0.02 mg/mL of resazurin (SRL) was made in DMEM media and 150  $\mu\text{L}$  of resazurin was added to every well of 96 well plate. After addition of resazurin, cells were incubated in the incubator for 6 hours and fluorescence readings were recorded (excitation wavelength - 520 nm and emission wavelength - 580 nm) in multimode plate reader. Percentage cell viability was calculated as follows, (fluorescence of treated cells -

fluorescence of media control)/ (fluorescence of DMSO controls – fluorescence of media control)) \* 100. Graphs were plotted by using non-linear regression curve fit programme of Graphpad Prism 9.0. EC<sub>50</sub> was calculated using Graphpad Prism software. The data provided are representative of three or four independent experiments.

**Combination cell viability studies in U2OS and Huh-7 cell line by CellTiter-Glo assay:** Cells were cultured and processed as discussed above. U2OS cells were treated with 10 uM to 0.0045 uM of IITK4001, IITK4003 and 100 uM to 0.045 uM of IITK4002, IITK4004, in combination with hydrogen peroxide - 150 µM, tert-Butyl hydroperoxide - 30 µM, Deferoxamine - 2 µM, Iron (II) perchlorate - 20 µM, Zinc triflate - 20 µM, Cobalt (II) chloride - 20 µM, Nickel perchlorate - 20 µM, staurosporine - 2 nM, QVD-OPh, - 10 µM, erastin - 0.5 uM. Huh-7 cells are treated with 1.1 µM, 0.37 µM, 0.123 µM of IITK4003, IITK4004 in combination with N-Acetylcysteine - 500 µM, α-tocopherol - 100 µM, Butathioninesulfoximine- 25 µM. 0.1% DMSO was used as negative control, 533 nM doxorubicin and 5 µM of cisplatin positive control conditions were used in the treatment. Cells were incubated for 72 hours at 37 °C, 5% CO<sub>2</sub> after treatment. After 72 hours of incubation, media was discarded from the wells and 30 µL of 1X CellTiter-Glo diluted in 1X PBS was added to all the wells in dark conditions and incubated at room temperature for 5 minutes. The 384 well plate was centrifuged for 1 minute at 1000 RPM and luminescence readings were recorded in multimode plate reader. Percentage cell viability was calculated as ((luminescence of treated cells - luminescence of media control)/ (luminescence of DMSO controls – luminescence of media control)) \* 100. Bar graphs were plotted by using the Graphpad Prism 9.0 software. The data provided are representative of three or four independent experiments.

**Combination cell viability assay in U2OS and Huh-7 cell line by Resazurin assay:** Cells were cultured and processed as discussed above. U2OS cells were treated with 10 uM to 0.0045 uM of IITK4001, IITK4003 and 100 uM to 0.045 uM of IITK4002, IITK4004 separately, in combination with QVD-OPh - 10 µM, RSL3 - 500 nM, ferrostatin - 10 µM, necrostatin -10 µM. 0.1% DMSO was used as negative control, 533 nM doxorubicin and 5 µM of cisplatin positive control conditions were used in the treatment. Cells were incubated for 72 hours at 37 °C, 5% CO<sub>2</sub> after treatment. After 72 hours of incubation, media was discarded from the wells and washed with 1X PBS. 0.02 mg/mL of resazurin (SRL) was made in DMEM media and 150 uL of resazurin was added to every well of 96 well plate. After addition of resazurin, cells were incubated in the incubator for 6 hours and fluorescence readings were recorded (excitation wavelength - 520 nm and emission wavelength – 580 nm) in multimode plate reader. Percentage cell viability was calculated as ((fluorescence of treated cells - fluorescence of media control)/ (fluorescence of DMSO controls – fluorescence of media control)) \* 100. Graphs were plotted by using non-linear regression curve fit programme of Graphpad Prism 9.0. EC<sub>50</sub> was calculated using Graphpad Prism software. The data provided are representative of three or four independent experiments.

**Mitochondrial ROS accumulation and its membrane potential analysis in Huh-7 cell line:** For mitochondrial membrane potential analysis, 25000 cells per well were plated in clear

flat bottom 96 well plates (NEST) in 200  $\mu$ L DMEM. Plates were incubated at 37 °C and 5% CO<sub>2</sub> for 24 hours. Post 24 hours of incubation, cells were treated for 90 minutes at 37 °C and 5% CO<sub>2</sub> with 0.02% DMSO, IITK4003- 20  $\mu$ M, IITK4004-20  $\mu$ M, H<sub>2</sub>O<sub>2</sub> - 150  $\mu$ M, JCHD- 150  $\mu$ M, IITK4003 + H<sub>2</sub>O<sub>2</sub>, IITK4004 + H<sub>2</sub>O<sub>2</sub>. Post 90 minutes, compounds from the wells were removed and wells were washed once with 100  $\mu$ L 1X PBS. Each well of cells were treated with 50  $\mu$ L of media that contains 30 nM Tetramethyl rhodamine, methyl ester percholate (TMRM) - (TCI) and 1 $\mu$ g/mL Hoechst 33342 (Thermo) and 1  $\mu$ M MitoSOX green (Invitrogen) for 30 minutes at 37 °C and 5% CO<sub>2</sub>. After incubation, media was removed from wells and wells were washed with 100  $\mu$ L 1X PBS for twice. 100  $\mu$ L 1XPBS was added to all wells and cells were observed under microscope and images were captured using fluorescent microscope (Bio-Rad ZOE fluorescent cell imager). Images were merged using ImageJ software. Bar graphs were plotted by using the Graphpad Prism 9.0 software. The data provided are representative of three or four independent experiments.

**ROS quantification by using DCFDA in U2OS and Huh-7 cell lines:** For measurement of total intracellular ROS levels in U2OS cells, 25000 cells per well were plated in clear flat bottom 96 well plates in 200  $\mu$ L DMEM. Plates were incubated at 37 °C and 5% CO<sub>2</sub> for 24 hours. Post 24 hours, cells were treated for 90 minutes at 37 °C and 5% CO<sub>2</sub> with 0.02% DMSO, tert-Butyl hydroperoxide - 60  $\mu$ M in U2OS and 100  $\mu$ M in Huh-7, H<sub>2</sub>O<sub>2</sub> - 150  $\mu$ M, NAC - 500  $\mu$ M, IITK4001 - 20  $\mu$ M, IITK4002 - 20  $\mu$ M, IITK4003 - 20  $\mu$ M, IITK4001 + H<sub>2</sub>O<sub>2</sub>, IITK4001 + tert-Butyl hydroperoxide, IITK4001 + NAC, IITK4002 + H<sub>2</sub>O<sub>2</sub>, IITK4002 + tert-Butyl hydroperoxide and IITK4002 + NAC, IITK4003 + H<sub>2</sub>O<sub>2</sub>, IITK4003 + tert-Butyl hydroperoxide and IITK4003 + NAC, IITK4004 + H<sub>2</sub>O<sub>2</sub>, IITK4004 + tert-Butyl hydroperoxide, IITK4004 + NAC, IITK4004 + H<sub>2</sub>O<sub>2</sub>, IITK4004 + tert-Butyl hydroperoxide. Post 90 minutes, 2  $\mu$ M of 2',7'-Dichlorofluorescein 3',6'-diacetate (DCFDA) (Thermo) (dissolved in DMSO) was directly added to cells and incubated in the incubator for 5 minutes. Media was removed from the wells and cells were washed with 100  $\mu$ L of 1X PBS for twice, cells were observed under microscope and images were captured using fluorescent microscope (Bio-Rad ZOE fluorescent cell imager).

**ATP quantification in U2OS and Huh-7 cell lines by using CellTiter-Glo reagent:** For the quantification of Adenosine-5' triphosphate in Huh-7, ATP magnesium salt (sigma) standard curve generation experiment was performed. 8 different concentrations of ATP were prepared in 1X PBS in triplicates as follows, 100  $\mu$ M, 25  $\mu$ M, 6.25  $\mu$ M, 1.56  $\mu$ M, 0.39  $\mu$ M, 0.097  $\mu$ M, 0.024  $\mu$ M, 0.006  $\mu$ M. 3X CellTiter-Glo reagent was added to all these ATP samples (final concentration - 1X) in white bottom 96 well plate. The luminescence readings were recorded in multimode plate reader. Luminescence readings of only 1X CTG was subtracted from all luminescence readings of various concentrations of ATP. XY scatter graph was plotted in microsofot excel by taking concentrations of ATP on X-axis and luminescence readings on Y-axis. Straight line equation, Y=mX+C was obtained from the graph. For measurement of total intracellular ATP levels in cells, 20,000 cells per well in 200  $\mu$ L DMEM were plated in white flat bottom 96 well plates. Plates were incubated at 37 °C and 5% CO<sub>2</sub> for 24 hours. Post 24 hours, Huh-7 cells were treated with 50  $\mu$ M, 30  $\mu$ M, 10  $\mu$ M of IITK4001 and IITK4003 and 30  $\mu$ M, 10  $\mu$ M, 1  $\mu$ M of IITK4002 and IITK4004, 200 nM of Antimycin A,



300 nM of rotenone, 1 mM of sodium azide. After incubation, media was removed from wells, 75  $\mu$ L of 1X CellTiter-Glo reagent was added to each well incubated at room temperature for 10 minutes and luminescence readings were taken by using multimode plate reader. Luminescence readings of only 1X CTG was subtracted from all other luminescence readings. Concentrations of ATP in U2OS cells which were treated with various concentrations of compounds were calculated by using  $Y=mX+C$  equation of ATP standard curve, where Y was luminescence reading, m was slope, X was concentration of unknown ATP and C was constant. The data provided are representative of three or four independent experiments.

**Extracellular ROS quantification with catalase and superoxide dismutase by using Amplex Red in Huh-7 cell line:** For the quantification of extracellular ROS,  $H_2O_2$  standard curve generation experiment was performed. 8 different concentrations of  $H_2O_2$  were prepared in 50  $\mu$ L of 0.5X PBS in triplicates as follows, 5  $\mu$ M, 1.6  $\mu$ M, 0.55  $\mu$ M, 0.18  $\mu$ M, 0.061  $\mu$ M, 0.02  $\mu$ M, 0.006  $\mu$ M, 0.002  $\mu$ M. 50  $\mu$ L of 50  $\mu$ M of Amplex Red (Thermo) and 0.1 U/mL of Horse Radish Peroxidase enzyme (sigma) in 0.5X PBS was added to all the wells of 96 well plate. The fluorescence readings at excitation wavelength 530 nm and emission wavelength 590 nm were recorded in multimode plate reader. Fluorescence readings of only 50  $\mu$ M of Amplex Red and 0.1 U/mL of HRP in 0.5x PBS was subtracted from all fluorescence readings of various concentrations of  $H_2O_2$ . XY scatter graph was plotted in microsofot excel by taking concentrations of  $H_2O_2$  on X-axis and fluorescence readings on Y-axis. Straight line equation,  $Y=mX+C$  was obtained from the graph. For the measurement of total extracellular ROS, Huh-7 cells were scrapped from T75 flask and the DMEM media was removed by centrifugation (2000 RPM for 3 minutes). 20000 cells in 50  $\mu$ L 0.5x PBS per well were plated in clear bottom 96 well plate (NEST). Cells were treated immediately with 20  $\mu$ M, 10  $\mu$ M, 5  $\mu$ M of IITK4003 and IITK4004, hydrogen peroxide- 5  $\mu$ M, and the combination of IITK4003, IITK4004 and hydrogen peroxide. All the conditions are further treated with 100 U/mL of catalase (Merck) and 4 U/mL of superoxide dismutase (Merck) separately. 0.02% DMSO was used as negative control. Post treatment, cells were incubated in the incubator (5%  $CO_2$ , 37  $^{\circ}C$ ) for 1 hour. After incubation, 50  $\mu$ M of Amplex Red and 0.1 U/mL of HRP were added to all the wells and incubated again for 1 hour in the incubator. Post incubation, fluorescence readings at excitation wavelength 530 nm and emission wavelength 590 nm were recorded in multimode plate reader. Fluorescence readings of only Amplex Red and HRP in 0.5x PBS were subtracted from all fluorescence readings of various treated conditions. Concentrations of  $H_2O_2$  in various treated conditions were calculated by using  $Y=mX+C$  equation of  $H_2O_2$  standard curve, where Y was fluorescence reading, m was slope, X was concentration of unknown  $H_2O_2$  and C was constant. Bar graphs were plotted by using the Graphpad Prism 9.0 software. The data provided are representative of three or four independent experiments.

**Dihydroethidine (DHE) oxidation assay in Huh-7 cell line:** For the measurement of total ROS (superoxide radical anions), Huh-7 cells were scrapped from T75 flask and the DMEM media was removed by centrifugation (2000 RPM for 3 minutes). 10000 cells in 50  $\mu$ L 1X PBS per

well were plated in clear bottom 96 well plate (NEST). Cells were treated immediately with 20  $\mu$ M, 10  $\mu$ M, 5  $\mu$ M of IITK4003 and IITK4004, hydrogen peroxide- 5  $\mu$ M, and the combination of IITK4003, IITK4004 and hydrogen peroxide. All the conditions are further treated with 100 U/mL of catalase (Merck) and 4 U/mL of superoxide dismutase (Merck) separately. 0.02% DMSO was used as negative control. Post treatment, cells were incubated in the incubator (5% CO<sub>2</sub>, 37 °C) for 1 hour. After incubation, 50  $\mu$ M of 5-ethyl-6-phenyl-5,6dihydro-phenanthridine-3,8diamine (BLD Pharma) was added to all the wells and incubated again for 1 hour in the incubator. Post incubation, fluorescence readings at excitation wavelength 510 nm and emission wavelength 610 nm were recorded in multimode plate reader. Fluorescence readings of only DHE in 1X PBS were subtracted from all fluorescence readings of various treated conditions. Bar graphs were plotted by using the Graphpad Prism 9.0 software. The data provided are representative of three or four independent experiments.

**Apoptotic cell death assay by Propidium Iodide staining:** For propidium iodide staining, 25000 cells per well were plated in clear flat bottom 96 well plates (NEST) in 200  $\mu$ L DMEM. Plates were incubated at 37 °C and 5% CO<sub>2</sub> for 24 hours. Post 24 hours of incubation, U2OS and Huh-7 cells were treated for 12 hours at 37 °C and 5% CO<sub>2</sub> with 0.02% DMSO, IITK4001- 20  $\mu$ M, IITK4002 - 20  $\mu$ M, IITK4003- 20  $\mu$ M, IITK4004 - 20  $\mu$ M, staurosporine - 250 nM, QVD-OPh - 10  $\mu$ M, necrostatin - 10  $\mu$ M, and the combinations like IITK4003+QVD-OPh, IITK4003 + staurosporine, IITK4004 + QVD-OPh, IITK4004 + staurosporine, IITK4003 + Necrostatin, IITK4004 + Necrostatin, necrostatin + staurosporine, staurosporine + QVD-OPh. After incubation with compounds, fresh DMEM media with 5  $\mu$ g/mL propidium iodide (sigma) was added to the cells for 20 minutes and incubated in the incubator. Cells were observed under microscope and images were captured using fluorescent microscope (Bio-Rad ZOE fluorescent cell imager). Images were merged using ImageJ software. The data provided are representative of three or four independent experiments.

**Apoptotic cell death imaging by Annexin-V immuno staining:** For annexin-V immuno staining, 25000 cells per well were plated in clear flat bottom 96 well plates in 200  $\mu$ L DMEM and plates were incubated at 37 °C and 5% CO<sub>2</sub> for 24 hours. Post 24 hours of incubation, U2OS were treated for 8 hours at 37 °C and 5% CO<sub>2</sub> with 0.02% DMSO, IITK4001- 30  $\mu$ M, IITK4003- 30  $\mu$ M, IITK4004- 30  $\mu$ M, IITK4002 - 30  $\mu$ M, staurosporine - 300 nM. Post treatment, cells were washed with 1X PBS. 2  $\mu$ L of Annexin - V (Alexa flour 488 – Thermo) was added to cells in 100  $\mu$ L of annexin binding buffer (10 mM HEPES, 150 mM NaCl, 2.5 mM CaCl<sub>2</sub>). They were incubated for 20 minutes in the incubator and images were recorded. Huh-7 cells were treated for 4 hours at 37 °C and 5% CO<sub>2</sub> with 0.02% DMSO, IITK4004-30  $\mu$ M, IITK4002-30  $\mu$ M, IITK4001-30  $\mu$ M, IITK4003-30  $\mu$ M, staurosporine - 300 nM. Post incubation, cells were washed with 1X PBS. 2  $\mu$ L of Annexin - V (Alexa flour 488 – Thermo) was added to cells in 100  $\mu$ L of annexin binding buffer (10 mM HEPES, 150 mM NaCl, 2.5 mM CaCl<sub>2</sub>). They were incubated for 6 hours in the incubator. Cells were observed under microscope and images were captured using fluorescent microscope (Bio-Rad ZOE

fluorescent cell imager). The data provided are representative of three or four independent experiments.

**Immuno blotting:** For immuno blotting, 0.1M cells/well (U2OS and Huh-7) were plated in 6 well plate (NEST) and were incubated at 37 °C and 5% CO<sub>2</sub> for 24 hours. Post 24 hours of incubation, cells were treated for 4 and 8 hours at 37 °C and 5% CO<sub>2</sub> with 0.02% DMSO, IITK4004- 30 µM, IITK4002 - 30 µM, IITK4001- 30 µM, IITK4003 - 30 µM and 6 hours with staurosporine - 100 nM. Post treatment, media was removed, cells were washed with 2 mL of ice cold 1X PBS. 60 µL of 1X protease phosphatase inhibitor (Thermo Fischer) was added per well and cells were scrapped. After scrapping, cells were lysed by using probe sonicator and cell lysate was collected after centrifugation at 20,000g for 45 minutes at 4 °C. Protein was quantified by Bradford reagent (SRL) and BSA standard. 20 µg protein was resolved on a 4-12% polyacrylamide gel for 90 minutes at 130 V. The gel was transferred to PVDF membrane (bio-rad) for 12 hours at 40 V, 4 °C by using transfer buffer (1.452g Tris-base, 7.2g glycine in 800 mL distilled H<sub>2</sub>O+200 mL of 100% methanol). The membrane was washed for 10 minutes with distilled water. The membrane was cut according to the molecular weight of desired protein. The membranes were blocked for 1 hour with 5% skimmed milk (SRL) in 1X TBST (50 mL of 10x TBST (12.1g tris-base, 40g glycine in 500 mL dH<sub>2</sub>O at pH-7.6) + 450 mL dH<sub>2</sub>O + 250 µL Tween 20 (SRL)). After blocking, the membranes were washed thrice every 10 minutes with 1X TBST. Then the membranes were incubated with primary antibodies in 1% skimmed milk with 1X TBST, i.e., β-tubulin (Anti-Rabbit-1:500 dilution- Abgenex), caspase-3 (Anti-Rabbit-1:1000 dilution), cleaved caspase-3 (Anti-Rabbit-1:1000 dilution) and cleaved PARP-1 (Anti-Rabbit-1:1000 dilution) antibodies for overnight at 4 °C [caspase and PARP antibodies were gifted by Dr. Jayandhran and Dr. Bushra Ateeq of IIT Kanpur]. After incubation with primary antibody, the membranes were washed thrice every 10 minutes with 1X TBST. Then the membranes were incubated with anti-rabbit secondary antibody (1:5000 dilution) in 1% skimmed milk for 1 hour at room temperature. After incubation, the membranes were washed thrice every 10 minutes with 1X TBST. Then blots were developed by using 250 mM luminol, 90 mM P-Coumaric acid with 50% H<sub>2</sub>O<sub>2</sub>. The blots were visualized by using chemidoc instrument.

**TBARS - Lipid Peroxidation Assay:** For lipid peroxidation assay in Huh-7 cells, 0.35 million cells per well were plated in clear bottom 12 well plate (NEST) and incubated in the incubator (5% CO<sub>2</sub>, 37 °C) for 24 hours. They were treated in triplicate with DMSO, 20 µM of IITK4001, IITK4002, IITK4003, IITK4004 and 4 mM of Diethyl maleate for 6 hours in the incubator. Post treatment, cells were washed with ice cold 1X PBS. Cells were scrapped by adding 200 µL of 2.5% trichloroacetic acid (SRL) and centrifuged for 15 minutes at 13,000g. The supernatant was collected and 200 µL of 15% TCA and 500 µL of 0.67% thiobarbituric acid (TBA) (GLR) are added to the same. They were vortexed are heated at 95 °C for 30 minutes and allowed to cool down to room temperature. To all the samples, 500 µL of n-butanol (Rankem) was added and let the aqueous and organic phases got separated. 200 µL of organic phase of all the samples are added to various wells of clear bottom 96-well plate and fluorescence readings were recorded at excitation wavelength 530 nm and emission

Wavelength 550 nm in multimode plate reader. For the quantification of MDA, malondialdehyde tetrabutyl ammonium salt (sigma) standard curve generation experiment was performed. 5 different concentrations of MDA were prepared in 2.5% TCA in triplicates as follows, 2.5  $\mu$ M, 1.25  $\mu$ M, 0.625  $\mu$ M, 0.312  $\mu$ M, 0  $\mu$ M. To these, 100  $\mu$ L of 0.67% TBA was added and heated at 95  $^{\circ}$ C for 30 minutes. The samples were allowed to cool down and fluorescence readings were recorded as described above. Concentration of MDA in the samples was calculated by using  $Y=mX+C$  equation of MDA standard curve, where Y was fluorescence reading, m was slope, X was concentration of unknown MDA and C was constant. The data provided are representative of three or four independent experiments.

**Py-H2AX immunostaining:** For Py-H2AX immunostaining experiment in Huh-7 cells, 25000 cells per well were plated in clear bottom 12 well plate (NEST) and incubated in the incubator (5% CO<sub>2</sub>, 37  $^{\circ}$ C) for 24 hours. They were treated in triplicate with DMSO, 20  $\mu$ M of IITK4001, IITK4002, IITK4003, IITK4004 and 1  $\mu$ M of Doxorubicin for 2 hours in the incubator. Post treatment, cells were washed with 200  $\mu$ L of ice cold 1x PBS and fixed with 100  $\mu$ L of 4% formaldehyde for 15 minutes at room temperature. Then the cells were washed with 200  $\mu$ L of ice cold 1x PBS twice. Then 100  $\mu$ L of ice cold 100% methanol was added to the cells and incubated at -20  $^{\circ}$ C for 10 minutes. Again, the cells were washed with 200  $\mu$ L of ice cold 1x PBS for thrice. Py-H2AX (Cell Signalling Technology) was diluted in 1:50 ratio by using antibody dilution buffer (1% BSA in 1X PBS) and 50  $\mu$ L of diluted antibody was added to the cells and incubated for 1 hour in dark at room temperature. In the last 10 minutes, the cells were stained with 1  $\mu$ g/mL hoechst stain. Post staining, cells were washed thrice with ice cold 1X PBS and cells were observed under microscope and images were captured using fluorescent microscope (Bio-Rad ZOE fluorescent cell imager). The data provided are representative of three or four independent experiments.

**3D Cell culture:** For 3D culture, HepG2 cells were maintained in Dulbecco's modified Eagle's medium (DMEM, Himedia) supplemented with 10% fetal bovine serum (FBS, Gibco). All cultures were maintained at 37  $^{\circ}$ C with 5% CO<sub>2</sub>.

**3D culture using Sodium alginate bead:** For 3D culture, freshly harvested from 2D cells were encapsulated in ALG beads by the method described in previous studies (Sun et al., 2017 and Xiao-xi Xu et al., 2014). In brief, the cells ( $4 \times 10^6$  cells/ml alginate) were suspended in filtered sterilized 1.5% (w/v) sodium alginate solution. Then alginate solution with cells was extruded into CaCl<sub>2</sub> solution (102 mM) using a 21-gauge syringe pump. After gelation for 30 Min, alginate gel beads were washed thrice with DMEM and placed in 6 well plates with DMEM supplemented with 10% FBS at 37 $^{\circ}$ C in a humidified atmosphere of 5% CO<sub>2</sub> in the air for 5 days. The medium was replaced every other day until the cell spheroids are formed.

**In Vitro Cell Viability Assay of 3D cultures:** The cytotoxicity effect of IITK4004 and IITK4003 on HepG2 was screened by the MTT colorimetric method. Briefly, 3 beads/well were seeded in 96-well plates at 37 $^{\circ}$ C. Then, cell scaffolds were treated with different concentrations of IITK4004 and IITK4003 (100 mM-1 nM) were added in the triplicate wells and incubated for 24 and 48 h time points. Mitomycin (10 mg/mL) is used as a positive control. After the specific times of exposure to extracts, the 3D cell spheroids were harvested from alginate

beads by simply treated with Citrate buffer 55 mM/EDTA 50 mM, pH 7.4, and then resuspended in a culture medium. Then plates were centrifuged at 2000 rpm for 10 minutes and discarded supernatant. Then cells were incubated with a final concentration of 5 mg/mL MTT solution. After 4 h incubation, the culture medium was replaced with 100  $\mu$ L of DMSO to dissolve the formazan crystals. The absorbance was read at 570/640 nm using a Tecon plate reader. The percentage of cell viability was determined, and graphs were plotted with GraphPad Prism 8.0.2.

**Synthesis of polymeric nanocarriers:** Polymeric nanocarriers were prepared using a water-in-oil-in-water double emulsion method described elsewhere, previously [1]. A 10 mg amount of carboxylic acid poly (ethylene glycol)-block-poly(lactide-co-glycolide) (PLGA-b-PEG-COOH) (Sigma-Aldrich) polymer was dissolved in dichloromethane and mixed with acetonitrile solution of drugs IITK4003 or IITK4004 (1.6 mg). Thereafter, this mixture was further mixed with 100  $\mu$ L of water and emulsified in an ice bath with a probe sonication for 45 s at 40% power rate. Then, 4 mL of 1.25% (w/v) sodium cholate solution dissolved in water, the biphasic mixture, was further emulsified for 3 minutes under similar conditions. Organic solvents were evaporated in a rotary evaporator under reduced pressure. The final volume of the nanocarrier suspension was made up to 5 mL by adding Milli-Q water. At this point the concentration of added IITK4003 was 350.6  $\mu$ M and IITK4004 was 267.55 $\mu$ M. Free drug molecules were separated by dialysis using a dialysis tube with molecular weight cut off 2000 Da (Sigma-Aldrich) with continuous stirring for 4h at 650 RPM.

**Characterization of polymeric nanocarriers:** The hydrodynamic diameter of the nanocarriers (with or without loaded drugs) were measured at 10 % (v/v) dilution in water using a NanoBrook 90 Plus particle analyzer (Brookhaven Instruments).

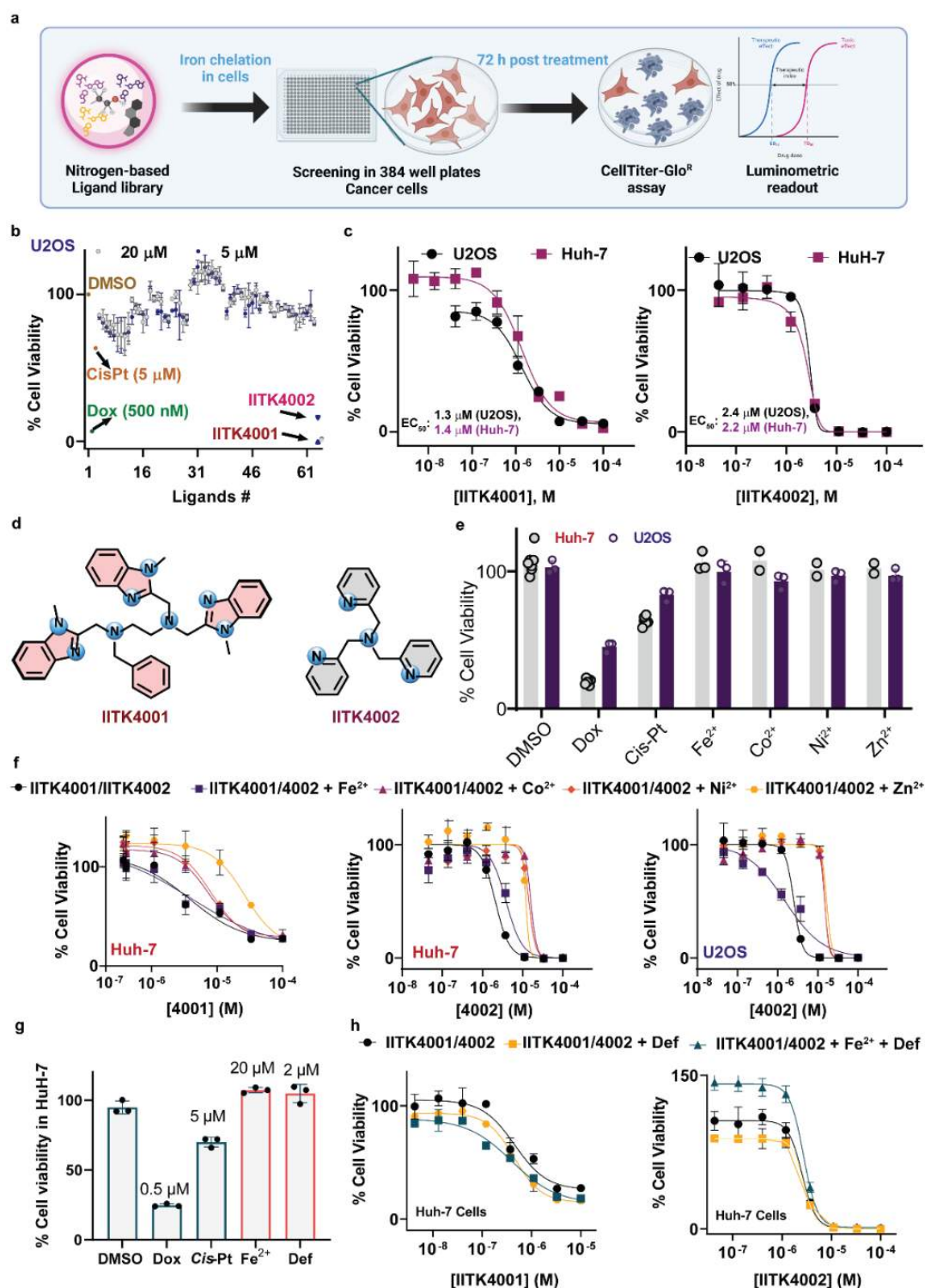
**Quantification of drug loading:** The amount of loaded drug in the polymeric nanocarriers was quantified by measuring the absorbance of the drug at 380 nm for IITK4003 and 360 nm for IITK4004. Briefly, a 20  $\mu$ L aliquot of drug loaded polymeric nanocarriers was diluted in 180  $\mu$ L of acetonitrile and placed in an ultrasonic bath for 30 minutes for disassembling the nanocarriers and simultaneously releasing the drug in the organic solvent. The concentration of the released drug was interpolated through regression analysis from standard curve of absorbance vs. known concentrations of the drug

## Results

### **IITK4001 and IITK4002 traps iron and complexes to prevent cancer cell proliferation:**

We first synthesized ligand scaffolds (di, tri, tetra, and penta-dentate) on one condition they are not planar but possess versatile three-dimensional orientations to resist DNA intercalation. Our screening of a ligand library (75 scaffolds, 20 and 5  $\mu$ M) identified two hit molecules, N'-benzyl-N',N''-(tris-N-methylbenzimidazole)-ethylenediamine, IITK4001 and tris(2-pyridylmethyl)amine, IITK4002 as a potent inhibitor of osteosarcoma (U2OS) cell proliferation (Figure 1a,b). Both IITK4001/4002 dose-dependently inhibited the proliferation of hepatocellular carcinoma (Huh-7) and U2OS cell growth with a range of 1-2  $\mu$ M EC50 (Figure 1c,d). These are nitrogen-based heterocyclic molecules, capable of acting as chelators

for various metal ions,<sup>25</sup> therefore, we determined to investigate the role of metal complexation with 3d-metals (iron, cobalt, nickel and zinc) in the antiproliferative activity of IITK4001 and IITK4002. Hence, we cotreated the cells with our lead molecules and indicated metal salts at non-toxic concentrations (20  $\mu$ M, Figure 1e). Interestingly, iron-salts cotreatment with both IITK4001/ IITK4002 retained the antiproliferative potential, however, other metal salts were found to suppress the activity of ligands IITK4001/ IITK4002 when combined (Figure 1f). Next, to investigate whether iron depletion using our metal ion



chelators in cells alone is sufficient to prevent cancer cell proliferation, we performed combination experiments with deferoxamine (Def, an iron chelator, Figure 1g, S21, S22) at the non-toxic concentration (2  $\mu$ M). We observed no substantial change in the cell survival in combination when compared to the lone treatment conditions. Yet, the addition of excess iron salt to IITK4001/4002 or in combination with Def did not rescue the cell death (Figure 1h). Therefore, we concluded the causative agent of cell death is unlikely to be iron depletion, but rather a shift in the free iron pool to form a complex of IITK4001/4002 and a possibility of additional roles for these iron complexes in the antiproliferative activity anticipated.

**Figure 1. IITK4001 and IITK4002 promote antiproliferative activity against Huh-7 and U2OS cells with iron salt.**

(A) Schematic flow of ligand screening in a cell viability assay using a luminescence-based Celltiter-Glo® assay after 72 hours of treatment.

(B, C, E, F) Cell viability data of (b) ligand library (#75) at 20 and 5  $\mu$ M (U2OS cells), (c) IITK4001 and IITK4002 in a dose-dependent fashion (U2OS and Huh-7), (e) metal salts alone and (f) in combination with IITK4001 or IITK4002.

(D) Structures of IITK4001 and IITK4002.

(G, H) Antiproliferative activity of IITK4002 in combination with deferoxamine (Def) and iron salt in Huh-7 cells. All graphs indicate mean  $\pm$  s.d. Data presented are performed in two independent cell lines and are representative of more than two independent experiments with a minimum of three technical replicates

**Cross complexation studies of IITK4002 with Fe<sup>2+</sup> and other biologically relevant metal ions:**

The initial examination of IITK4001 and IITK4002 led to the conclusion of iron complex formation rather than iron depletion as the dominant mechanism for preventing cancer cell proliferation. However, other metal ions in the biological system could potentially interfere with the activity. Therefore, we assembled salts of various metal ions around their physiological concentrations including alkali metals, 5 millimolar solution of sodium, magnesium, potassium, calcium salts, and d-block transition metals such as manganese (1  $\mu$ M), iron (20  $\mu$ M), cobalt (0.5  $\mu$ M), nickel (0.5  $\mu$ M), copper (5  $\mu$ M) and zinc (100  $\mu$ M) salts (Figure 2).<sup>22</sup> Due to the solubility issues with IITK4001 under physiological conditions, we restricted all our cross-complex formation studies with IITK4002 (Figures 2, S6, S7). Initially, we monitored the Fe(II)-IITK4002 formation with 0.2 to 2.0 equiv. of IITK4002 using UV-visible spectroscopy by following a distinct absorption at 395 nm (Figure 2a-c). We find an instant complex formation upon the addition of Fe<sup>2+</sup> to IITK4002, and this was found to be saturated with 1: 1 stoichiometry, indicating the 1 to 1 complex formation. This complex was found to be irreversible and stable in the complexation medium for more than an hour (Figure 2a,b). To study the interference of assembled biologically relevant metal ions, an excess of these metal salts (5 equiv.) was added to the preformed Fe(II)-IITK4002 complex and monitored the change in absorbance at 395 nm. We observed no effect with any of the alkali metal ions and also with transition metal ions such as Mn<sup>2+</sup>, Ni<sup>2+</sup>, and Co<sup>2+</sup> salts indicating Fe(II)-IITK4002 complex is irreversible under these conditions (Figure 2e). However, we find a slow equilibration of Fe(II)-IITK4002 with Zn<sup>2+</sup> over 60 min to a ~50% Fe(II)-IITK4002 (Figure 2f). Conversely, the reverse addition of Fe<sup>2+</sup> salt to preformed Zn(II)-IITK4002 exhibited a rapid displacement of Zn<sup>2+</sup> within a few seconds ( $t_{1/2}$  = 4 s) to form Fe(II)-IITK4002 and observed a slow equilibration over 60 min (Figure 2g), thereby suggesting the complex is competitively reversible. Identical to this, the addition of Cu<sup>2+</sup> was found to react instantly with Fe(II)-



IITK4002 that in less than 20 seconds all the Fe(II)-IITK4002 converted into Cu(II)-IITK4002 ( $t_{1/2}$  = 8.3 s, Figure 2h, i) and was found to equilibrate to nearly 50% in 6 min. Likewise, the reverse addition also exhibited a similar trend of instant conversion of Cu(II)-IITK4002 to Fe(II)-IITK4002 transformation was observed ( $t_{1/2}$  = 3.2 s, Figure 2j). Together, the cross-complexation studies of Fe(II)-IITK4002 with biologically relevant metal ions indicate that  $\text{Zn}^{2+}$  and  $\text{Cu}^{2+}$  could potentially interfere and remain unaffected with other metal ions tested. While the physiological concentration of copper ( $0.5\ \mu\text{M}$ ) is four-fold lesser than iron concentration ( $20\ \mu\text{M}$ ), zinc ( $100\ \mu\text{M}$ ) is found to be 20-fold higher levels than iron. Despite higher levels of  $\text{Zn}^{2+}$  in the biological systems, we have observed addition of  $\text{Zn}^{2+}$  to IITK4001 showed more of a preventive role than retaining or enhancing the cell death induced by IITK4002 (Figure 1f). The above set of experiments has clearly ruled out the majority of the biologically relevant metal ions except for a competition between  $\text{Fe}^{2+}$  and  $\text{Cu}^{2+}$ . Therefore, evaluating the individual effects of  $\text{Fe}^{2+}$  and  $\text{Cu}^{2+}$  ions on IITK4002 is essential to precisely capture the metal ion responsible for the antiproliferative activity of our lead ligand molecules.

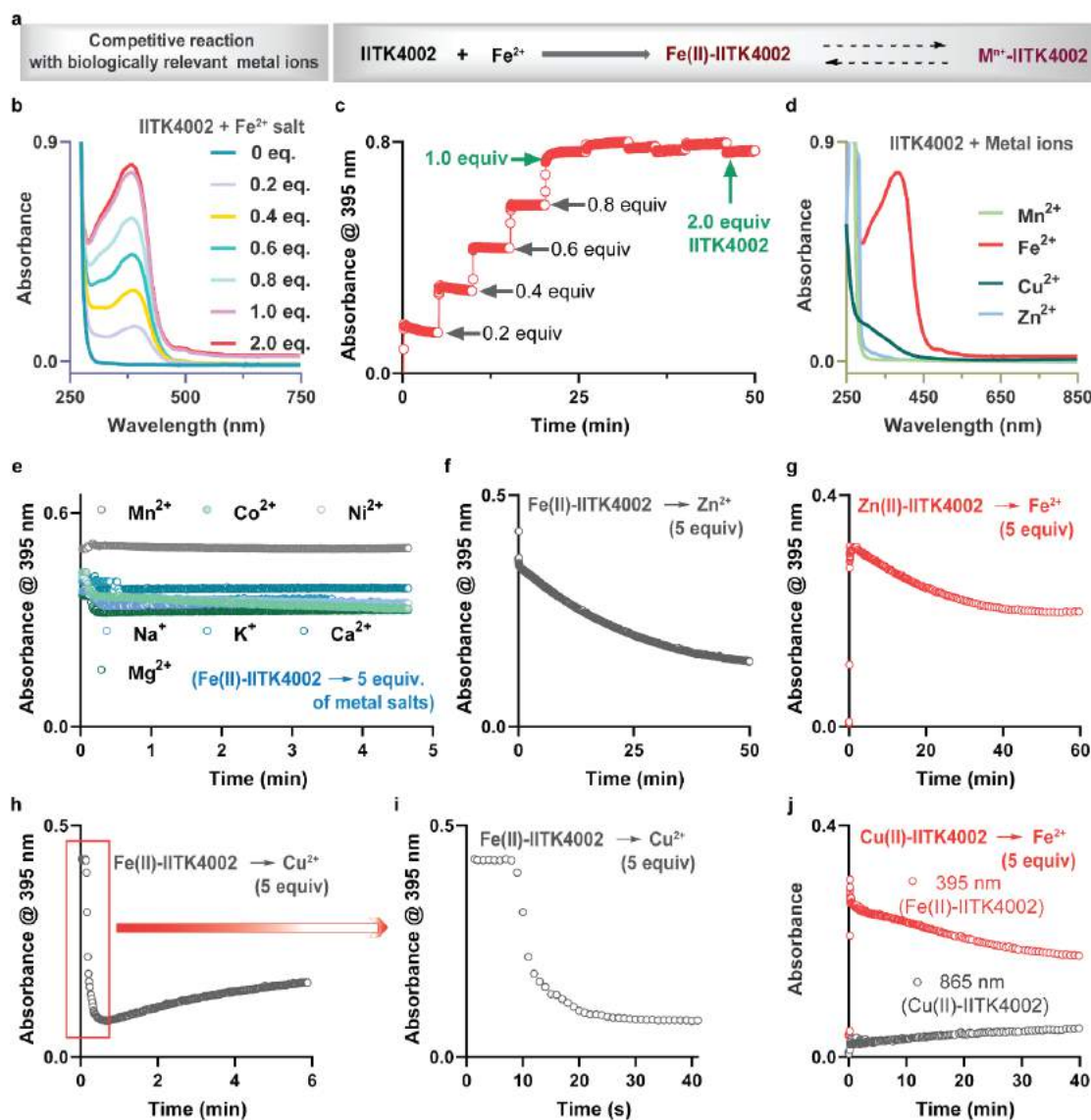


**Figure 2. Fe(II)-IITK4002 is competitively reversible with  $\text{Zn}^{2+}$  and  $\text{Cu}^{2+}$  salts.**



(A) Scheme for competitive complexation studies for IITK4002 with Fe<sup>2+</sup> and other metal ions.

(B-D) UV-visible spectra of IITK4002 with Fe<sup>2+</sup> salt (0 to 2.0 equiv.) and other metal salts (1 equiv.) in 1:1 acetonitrile: water at RT.

(E, F, H, I) Absorbance was recorded at 395 nm for Fe(II)-IITK4002 after exposing it to indicated metal salts (5 equiv.) at RT.

(G,J) Zn(II)-IITK4002 (g) or Cu(II)-IITK4002 (j) complex exposed to Fe<sup>2+</sup> salt (5 equiv.) at RT and absorbance recorded at 395 nm for the Fe(II)-complex formation

### **Synthesis and physio-chemical evaluation of iron complexes (IITK4003 and IITK4004) and other 3d-metal complexes:**

Iron and copper are indispensable elements for redox homeostasis in cells due to their versatile redox capacity to switch between multiple oxidation states.<sup>5,21-23,26-29</sup> Next, we set out to investigate whether the effect of our ligands is due to their complexation with Fe<sup>2+</sup> or Cu<sup>2+</sup>. To unambiguously characterize this, we synthesized the iron complexes IITK4003 and IITK4004 and characterized them by various spectroscopic techniques and X-ray crystallography studies (Figure 3, scheme 1-2 S1-5, Table S1).<sup>29-31</sup> Iron complexes IITK4003 and IITK4004 were found to show comparable growth inhibition activity against both Huh-7 and U2OS cells as in the ligands treatment alone (Figure 3a, b). Remarkably, IITK4003 exhibited an exceptional antiproliferative activity with an EC<sub>50</sub> of 340 nM against Huh-7 cells, a 3-fold better than the parent ligand IITK4001 (Figure 3a). This difference in potency could be partially attributed to the better solubility of the complex over the ligand in aqueous conditions. Next, we synthesized authentic metal complexes of IITK4002 with other 3d-metal salts, Co<sup>2+</sup> (IITK4005), Ni<sup>2+</sup> (IITK4006), Cu<sup>2+</sup> (IITK4007) and Zn<sup>2+</sup> (IITK4008) (Figure 3c). The complexation of these 3d-metal ions with IITK4001 failed due to experimental difficulty in crystallizing and obtaining pure complexes. Then, we have evaluated for their ability to prevent the growth of Huh-7 and U2OS in a dose-dependent fashion. Next, in our evaluation for the antiproliferative activity of IITK4005 and IITK4006, both were found to be non-toxic even at 100 μM concentrations (Figure 3c-e), suggesting Co<sup>2+</sup> and Ni<sup>2+</sup> complexation are unlikely to be responsible for the ligand's antiproliferative activity. Interestingly, two of the metal ions found to be competitive in complexing with IITK4002, Cu<sup>2+</sup> (IITK4007) and Zn<sup>2+</sup> (IITK4008) exhibited a weak potency (5.4 μM, 7.0 μM in Huh-7 and 12.8 μM and >50 μM in U2OS for IITK4007 and IITK4008 respectively) in preventing the growth of cancer cells evaluated. However, the antiproliferative potencies were significantly lower than the parent ligand alone or the respective iron complex, IITK4004 (Figure 3c-e). Together, the evaluation of metal complexes and the combination of various metal salts with heterocyclic ligands highlight that their antiproliferative activity arises predominantly due to iron complex formation in cells. Next, we extended the cell viability assay in the human embryonic kidney (HEK293) to estimate the selectivity index (SI) of our lead complexes (IITK4003 and IITK4004). We recorded an EC<sub>50</sub> of 3.82 μM for IITK4003 with HEK293 cells, an estimated SI of 9.0 (EC<sub>50</sub> in 0.34 μM), and an SI of 3.4 for Huh-7 cells (EC<sub>50</sub>: 7.6 μM with HEK293 cells and 2.2 μM with Huh-7 cells, Figure 3f). Overall, IITK4003/4004 showed better selectivity in preventing liver cancer cells' growth (Huh-7) over normal kidney cells. These studies together suggested that

the complexation of iron with IITK4001/4002 is a major determinant factor for the antiproliferative action in Huh-7 and U2OS cells.

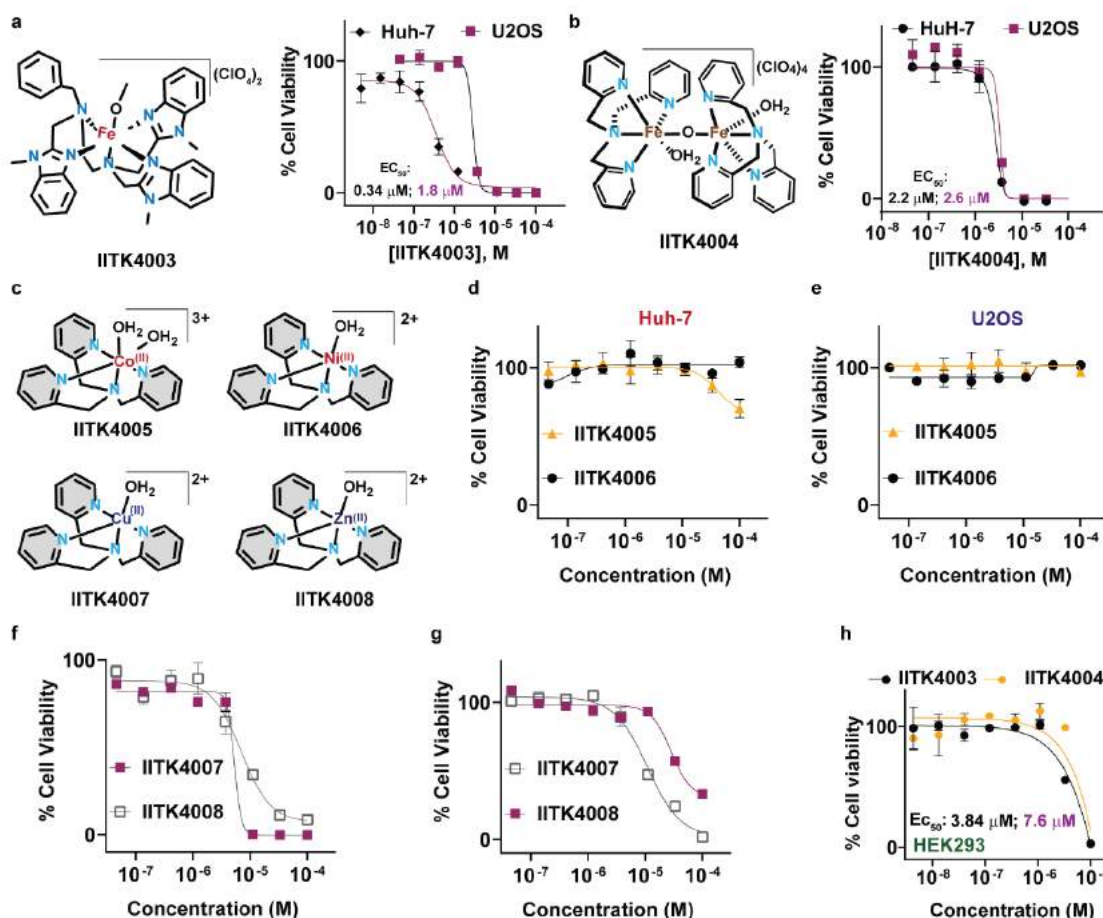


**Figure 3. Iron complexes (IITK4003/4004) exhibit potent antiproliferative activity over other metal complexes in Huh-7 cells.**

(A-G) Cell viability of Huh-7 and U2OS cells assessed with IITK4003 (A), IITK4004 (B), IITK4005-4008 (D-G) using Celltiter-Glo® assay.

(A-C) Structure of complexes studied in here are presented.

(H) The toxicity of lead complexes, IITK4003/4004, to HEK293 cells was assessed in a dose-dependent fashion.

Graphs A, B, D-H indicate mean  $\pm$  s.d.

Data presented are performed in two independent cell lines and are representative of more than two independent experiments with a minimum of three technical replicates.

### **IITK4003/4004 generates reactive metal-oxo species under aqueous conditions:**

In addition to iron depletion, we anticipated a lead redox role for our top hits' mechanism of action in cells. The redox mechanisms of Fe(II)-complexes would generate reactive oxygen species (ROS) in cells to trigger redox imbalance. The delicate balance of redox homeostasis is essential for cancer cell survival and metastasis, which could be capitalized on for developing selective cancer therapeutics.<sup>32-34</sup> Therefore, we evaluated the redox reactivity of IITK4004 with peroxides in water (Figures 4a-d, and S7-11), a study thus far not investigated, majorly owing to the instability of reactive metal-oxo species in an aqueous milieu. While we expect the dinuclear-iron complex, IITK4004 to be electron paramagnetic resonance (EPR)

silent (due to antiferromagnetic coupling), we observed a high spin  $S = 5/2$  signal, indicative of monomeric  $[\text{Fe(III)}\text{-IITK4002}]^{3+}$  formation upon dissolution (Figure 4a,b, S11).<sup>35</sup> Our cyclic voltammetry (CV) studies of IITK4004 and *in situ* prepared  $\text{Fe(II)}\text{-IITK4002}$  in water exhibited a reversible redox wave at  $E_{1/2}$  0.4 V vs Ag/AgCl, whereas  $E_{1/2}$  of 1.2 V vs Ag/AgCl in acetonitrile indicating more facile oxidation in water (Figure 4a,b, S7). Next, we exposed IITK4004 in water to  $\text{H}_2\text{O}_2$  and observed a characteristic absorption for  $[(\text{IITK4002})\text{Fe(III)}\text{-OOH}]^{2+}$  species at 620 nm, and this species was also characterized using EPR spectroscopy (g values: 2.19, 2.14, and 1.97, Figure 4c).<sup>35-38</sup> Together these data indicate that IITK4004 produces a monomeric  $[(\text{IITK4002})\text{Fe(III)}\text{-OOH}]^{2+}$  species in water upon the interaction with  $\text{H}_2\text{O}_2$ . Unlike in acetonitrile (Figure S7-11), the  $[(\text{IITK4002})\text{Fe(III)}\text{-OOH}]^{2+}$  in water, converts temporally to  $[(\text{IITK4002})\text{Fe(IV)}=\text{O}]^{2+}$  with an absorption band at 720 nm (Figure 4c, d).<sup>39</sup> A similar set of reactivity patterns was observed for IITK4004 with *tert*-butyl hydroperoxide ( $t\text{BuOOH}$ ) to generate reactive oxidative species  $[(\text{IITK4002})\text{Fe(IV)}=\text{O}]^{2+}$  (Figure S8d, S10).<sup>40,41</sup> Further, we independently mixed IITK4002 with  $\text{Fe}^{2+}$  and  $\text{Fe}^{3+}$  salts for *in situ* formation of  $(\text{IITK4002})\text{Fe(II)}$  and  $(\text{IITK4002})\text{Fe(III)}$  complexes. To our delight, exposing them to  $\text{H}_2\text{O}_2$  and  $t\text{BuOOH}$  produced a similar  $\text{Fe(III)}\text{-OOH}$  and  $\text{Fe(III)}\text{-OO}^t\text{Bu}$ , respectively, which decayed to yield the highly reactive  $[(\text{IITK4002})\text{Fe(IV)}=\text{O}]^{2+}$  complex (Figure 4c, d, S11). A comparable study for IITK4003 capturing metal-oxo species formation (Figure S6) has strongly suggested that both complexes possess a strong oxidative capacity with peroxides under physiological conditions.

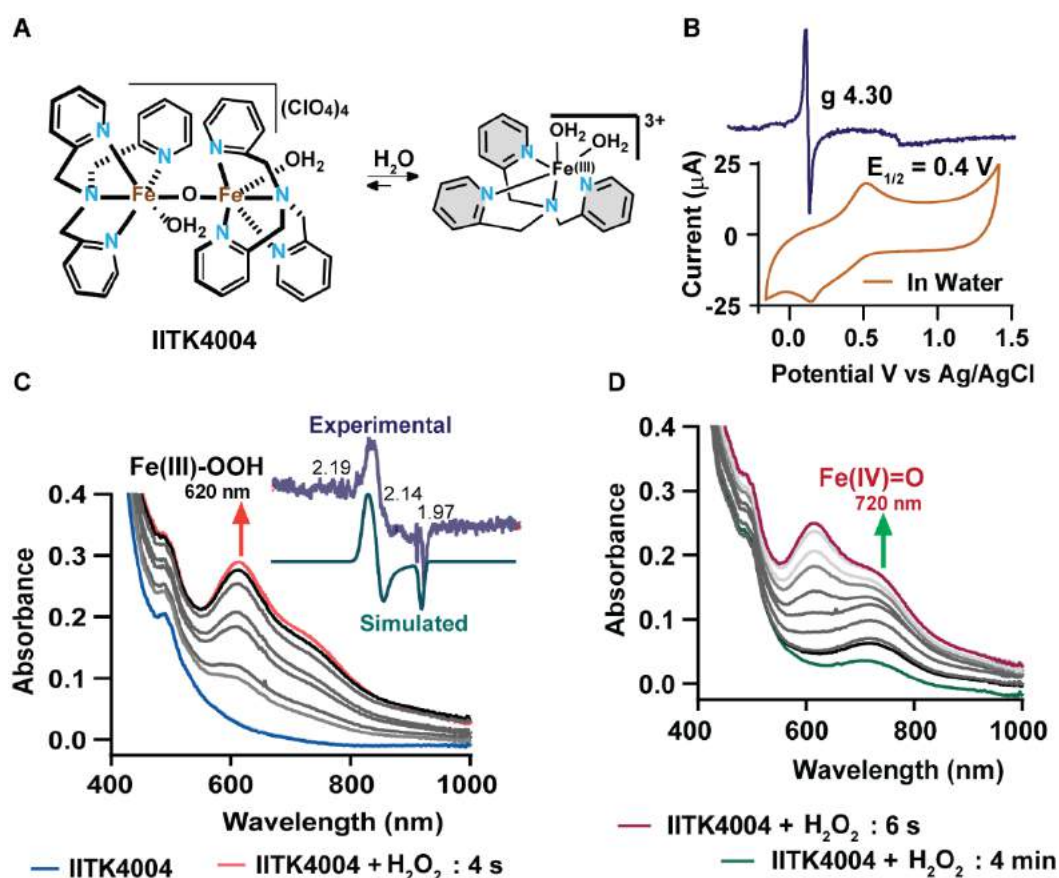


Figure 4. Iron complex, IITK4004 generates reactive metal-oxo species under simulated physiological conditions

(A, B) Monomerization of IITK4004 in water assessed using X-band EPR spectrum of IITK4004 in water/CH<sub>3</sub>CN at 120 K (insert) and cyclic voltammogram in water.

(C) UV/Vis absorption spectral studies depicting reactive meta-oxo species formation  $[(\text{TPA})\text{Fe}(\text{III})\text{-OOH}]^{2+}$  (620 nm) and its X-band EPR spectrum compared with simulated EPR spectrum (insert).

(D) The transformation of  $[(\text{TPA})\text{Fe}(\text{III})\text{-OOH}]^{2+}$  (620 nm) to  $[(\text{TPA})\text{Fe}(\text{IV})\text{=O}]^{2+}$  (720 nm) in a reaction of IITK4004 with H<sub>2</sub>O<sub>2</sub> (10 equiv.) in water is monitored using UV/Vis absorption spectral studies.

### **ROS generation by IITK4001-IITK4004 accumulates lipid peroxide but no sign of DNA damage:**

After establishing the formation of reactive iron-oxo intermediates with peroxides under *in vitro* conditions, we assessed the cellular ROS generation with our hits. Initially, we performed the amplex red<sup>®</sup> assay to quantify extracellular ROS upon treatment of Huh-7 cells with our lead molecules (5A-C).<sup>42</sup> Indeed, our lead molecules generated ROS extracellularly and addition of catalase enzyme (a quencher of hydrogen peroxide) or superoxide dismutase enzyme (SOD, converts superoxide radical anion, into hydrogen peroxide) had partial or minimal effect on the IITk4003/4004 induced ROS generation (Figure 5A-C). We also used another fluorescence-based assay, dihydroethidine (DHE) oxidation assay for ROS measurement. The DHE reacts with superoxide radical anion to generate 2-hydroxy ethidium and hydroxy radical to generate ethidium as oxidized products.<sup>42-44</sup> We observed a similar trend in ROS generation as in the amplex red<sup>®</sup> assay that our lead molecules profoundly generated ROS, whereas the ROS quenchers such as catalase or SOD exhibited no suppression of ROS levels (Figure 5D-F). These studies led to the conclusion that in addition to superoxide radical anion or hydrogen peroxide, the highly reactive metal-oxo species could generate other oxidized biomolecules and promote oxidative stress. Next, we assessed the intracellular ROS generation with our lead molecules alone or in combination with oxidant (H<sub>2</sub>O<sub>2</sub>) and antioxidant (*N*-acetylcysteine). We used a turn-on fluorescence-based H<sub>2</sub>DCF-DA oxidation assay in Huh-7 and U2OS cells to measure the intracellular ROS accumulation. We observed a sharp increase in the fluorescence intensity with IITK4003/4004 similar to H<sub>2</sub>O<sub>2</sub> treatment suggesting the accumulation of intracellular ROS. Conversely, combining our top hits with antioxidant, *N*-acetylcysteine (NAC) has rescued the ROS effect (Figure 5G, S13). Two of the most sensitive biomolecules to intracellular ROS accumulations are deoxyribonucleic acid (DNA) and lipid molecules. First, we assessed the lipid peroxidation in cells when exposed to our lead molecules. Peroxidation of polyunsaturated fatty acids (PUFA) is known to convert them into malondialdehyde (MDA), which could be trapped using condensation chemistry with thiobarbituric acid (TBA) (Figure 5H) with TBARS (thiobarbituric acid reactive substance) assay.<sup>45</sup> Quantification of MDA-TBA condensed product indicated a two-to-three-fold enhancement in the levels of lipid peroxides (Figure 5I, S14). Besides, DNA damage is a routine mechanism predicted when metal complex-mediated ROS generation is captured.<sup>46</sup> However, our analysis of H2AX protein phosphorylation at gamma position, a biomarker for DNA damage mechanism ( $\gamma$ -H2AX), using immunofluorescence imaging, displayed minimal or no effect compared to doxorubicin (Dox, Figure 5J, S15), thereby ruling out DNA damage mechanisms responsible for antiproliferative activity. Therefore, we concluded that the

cancer cell death induced by our lead molecules could potentially arise due to lipid peroxide accumulation rather than DNA damage-mediated mechanism.

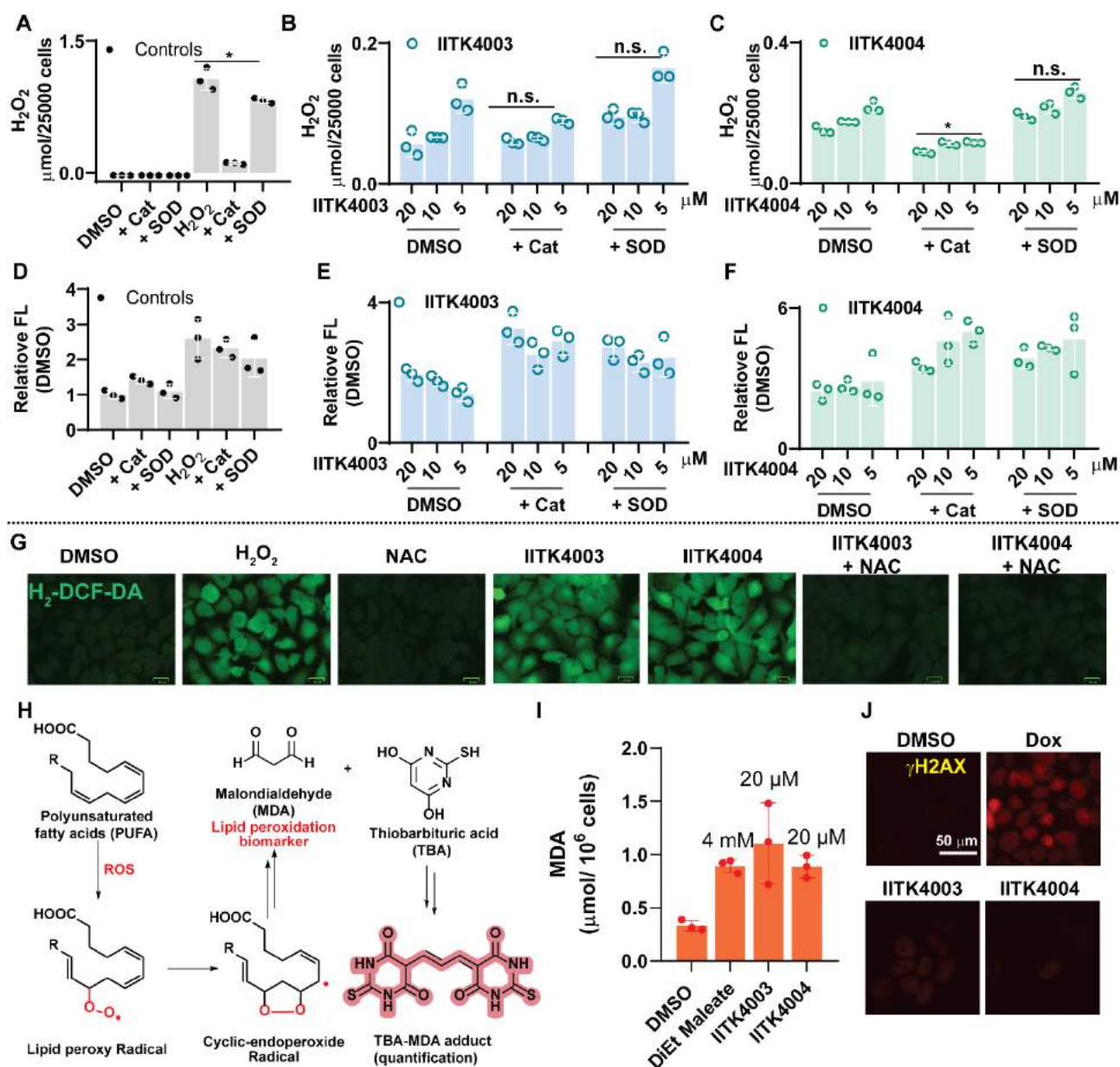


**Figure 5. Lead molecules accumulate lipid peroxide to induce oxidative stress in cancer cells**

(A-F) Extracellular ROS was quantified after the treatment of Huh-7 cells with IITK4003/4004 in combination with catalase and superoxide dismutase enzymes using fluorescence-based Amplex red® assay (A-C) and DHE oxidation assay (D-F).

(G) Intracellular ROS accumulation was visualized using  $H_2$ -DCFDA oxidation experiment. Scale bar: 25 μm.

(H, I) Schematic depicting polyunsaturated fatty acid (PUFA, lipid) peroxidation in cells

(H) and its quantification using TBARS assay (I).

(J) Immunofluorescence analysis of cell stained with anti-γH2AX upon treatment with doxorubicin (Dox) and lead molecules (20 μM). Scale bar: 25 μm.

Graphs A-F and I indicate mean ± s.d. Data presented are representative of more than two independent replicates and a minimum of three technical replicates

**Iron complexes accumulate lipid peroxide and do not induce ferroptosis:**

Thus far, the results of iron complexes enhancing intracellular ROS accumulation leading to lipid peroxidation have instinctively driven us to investigate the cell death mechanism of ferroptosis, an iron-dependent oxidative cell death induced through lipid peroxide accumulation.<sup>47</sup> Ferroptosis has been linked with multiple steps in the biosynthesis of glutathione and its redox cycling. For example, erastin is reported to inhibit cystine uptake to induce ferroptosis by targeting System Xc<sup>-</sup>, a cystine-glutamate antiporter system. RSL3 is a ferroptosis inducer that inhibits glutathione peroxidase 4 (GPX4), a lipid peroxidase enzyme employs glutathione for quenching lipid peroxides and directly inhibits ferroptosis (Figure S16A). Conversely, ferrostatin-1 (Fer-1) and liproxstatin-1 (Lip-1), are specific ferroptosis inhibitors that scavenge lipid peroxides and restore GSH levels (Figure S16A). We chose to combine these ferroptosis modulators with our lead molecules to witness the effect. Initial evaluation of canonical GPX4 inhibitor, RSL3 robustly inhibited the growth of Huh-7 cells with an EC<sub>50</sub> of 26 nM and its combination with either Fer-1 or Lip-1 showed a tremendous prevention effect by more than 500-fold, thereby validating the ferroptosis assay system (Figure S16C, D). Whereas, combining our hits (IITK4001-IITK4004) with either Fer-1 or Lip-1 did not provide any significant protective effect, (Figure S16D, F, and S17). Further, in our assessment, neither erastin nor RSL3 potentiated the cancer cell killing (in both Huh-7 and U2OS) by IITK4001-4004 (Figure S16b,c,f, S17), thus dismissing the possibility of a ferroptosis cell killing mechanism for IITK4001-4004. In addition, ROS-mediated cancer cell death is known to trigger necroptosis and rapid cellular damage. However, cancer cell viability analysis for our hits in combination with necrostatin-1 (necroptosis inhibitor) showed little cell death prevention (Figure S17) thereby eliminating this possibility as well.

**IITK4003/4004 induces mitochondrial dysfunction:**

Mitochondria, the powerhouse of cells is a sensitive organelle that responds to a sudden fluctuation of redox status. Upon exposure to toxic levels of ROS, mitochondrial membrane potential (MMP) is affected which could be measured using established TMRM (Tetramethylrhodamine methyl ester)-mitochondria imaging by the reduction in TMRM fluorescence intensity (Figure 6A, B and S18). We observed a considerable decrease in the labeling of mitochondria by TMRM in both Huh-7 and U2OS cells in the conditions treated with IITK4003/4004 and hydrogen peroxide alone or in combination (Figure 6A, B and S18). Identical to the H<sub>2</sub>DCF-DA assay, the cotreatment of IITK4003 or IITK4004 with peroxides and NAC, inversely correlated with their mechanism as expected (Figure 6A, B). In parallel, we used MitoSOX<sup>®</sup> green to capture the mitochondrial ROS accumulation (Figure 6A, C). We used a reported ROS generator and lipid peroxidation inducer, JCHD as a positive control (Figure 6A, C).<sup>42,43</sup> Our molecules on their own diminished the MMP and drove low levels of mitochondrial ROS accumulation, however, upon exposure to H<sub>2</sub>O<sub>2</sub>, a sharp increase in the overall ROS level was detected (Figure 6A, C). Overall, these findings suggest that IITK4003/4004 drives ROS accumulation which could impair mitochondrial function in cancer cells. Given that our lead molecules disrupt MMP and induce ROS accumulation in cells, we chose small molecule inhibitors of ETC complexes, rotenone (complex I),<sup>48</sup> antimycin A



(complex III)<sup>49</sup> and sodium azide (NaN<sub>3</sub>, complex IV)<sup>50</sup> to compare and assess the effect of IITK4003/4004 on mitochondrial function in cancer cells (Figure 6D, S19A, B). One of the outcomes of mitochondrial functional inhibition is the depleted ATP levels. Our quantification of ATP levels in Huh-7 cells with lead molecules and canonical ETC inhibitors exhibited a profound decrease in ATP assuring a parallel mitochondrial functional inhibition mechanism for IITK4003/4004 (Figure 6D, S19). Having established oxidative mitochondrial dysfunction in cells with our lead molecules, we set out to evaluate the effect of ROS modulators on the toxicity of IITK4003/4004 to Huh-7 cells. Therefore, we combined buthionine sulfoximine (BSO, a glutathione biosynthesis inhibitor, induces oxidative stress) and antioxidants (vitamin E (Vit-E) and NAC) with IITK4001-IITK4004 independently, to capture their effect on the proliferation of cancer cells (Figure 6E, F, S20). We observed a uniform trend of dose-dependent enhancement of cell death with BSO and a protective effect by Vit-E/NAC for all the molecules tested (Figure 6E, F). This is effectively suggesting oxidative stress induction is a relevant molecular mechanism of our lead molecules.

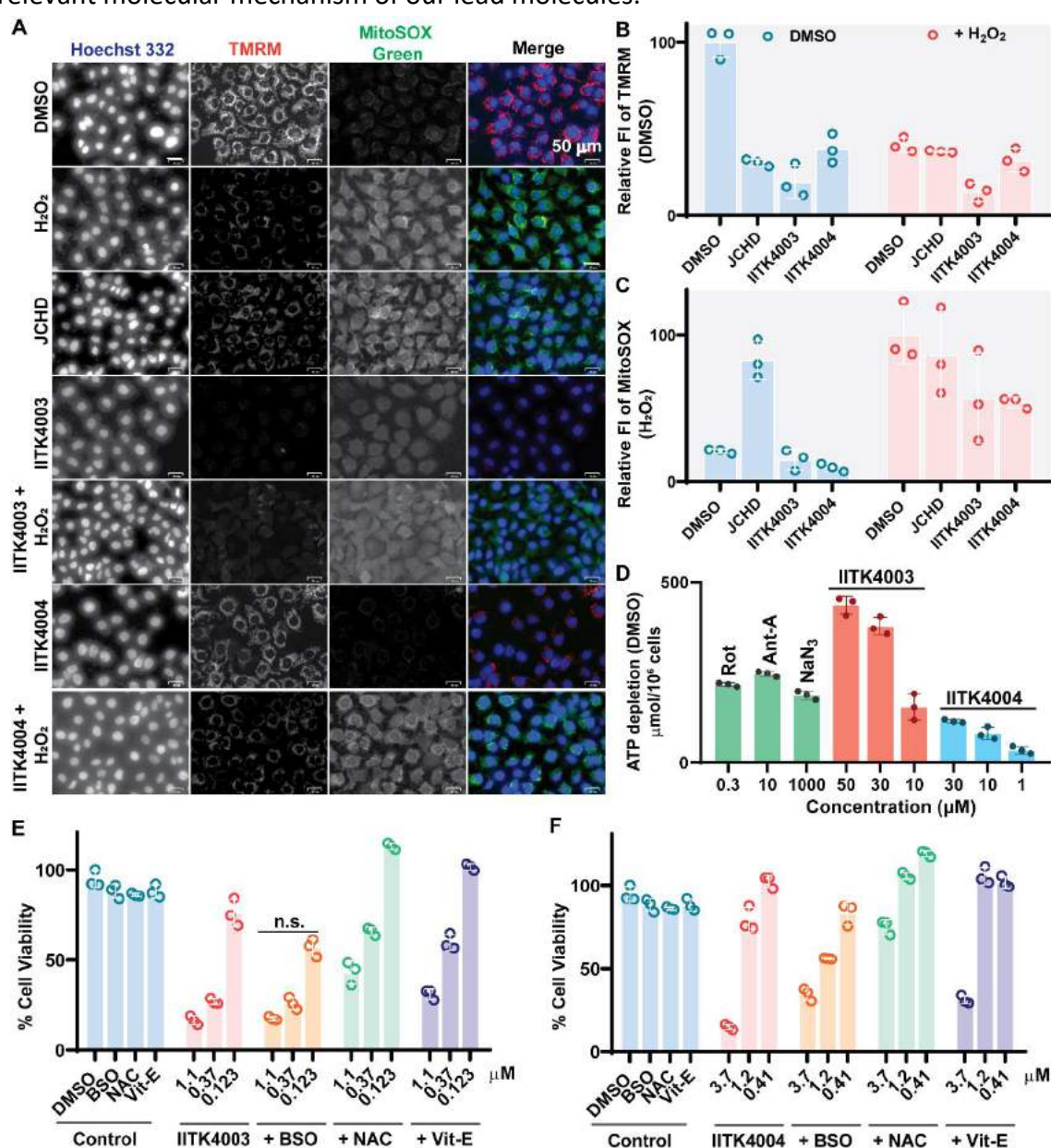


**Figure 6. IITK4003/ IITK4004 induced ROS accumulation led to mitochondrial dysfunction and correlated with ROS mediated Huh-7 cell death.**

(A-C) Effect of indicated compounds and combinations on MMP in Huh-7 cells imaged using a potentiometric fluorophore, TMRM and ROS accumulation with MitoSOX Green using fluorescence microscopy (A) and their relative fluorescence intensity quantified data (B, C). Scale bar: 25  $\mu$ M.

(D) Reduction in the levels of ATP quantified using a luminescence based Celltiter-Glo<sup>®</sup> assay in Huh-7 cells upon treatment with indicated molecules.

(E, F) Effect of additional non-toxic dose of oxidants (BSO-50  $\mu$ M) and antioxidant (Vit-E-300  $\mu$ M, NAC-500  $\mu$ M) on the cell viability of huh-7 cells treated with IITK4003 (E) or IITK4004 (F) at indicated concentrations

Graphs B-F indicate mean  $\pm$  s.d. Data presented are performed are representative of more than two independent replicates and a minimum of three technical replicates.

### **IITK4003/4004 trigger caspase cascade to induce apoptosis:**

Oxidative mitochondrial impairment leads to the release of mitochondrial proteins including Bcl-2, and cytochrome c into the cytosol, which are known to activate caspase cascade and trigger apoptosis.<sup>51-53</sup> Therefore, we used multiple sets of experiments including combination treatment cell viability studies, immunoblotting and immunofluorescence imaging to capture the cell death mechanism (Figure 7). First, we investigated the effect of staurosporine, an inducer of the programmed cell death mechanism, apoptosis, and an apoptosis inhibitor QVD-OPh (a pan-caspase inhibitor), in combination with our lead molecules in Huh-7 and U2OS cells (Figure 7A-D, and S22).<sup>54,55</sup> We observed profound rescue of cell death by QVD-OPh when combined with lead molecules and slight positive effect with Staurosporine, together hinting that apoptosis mechanism is likely (Figure 7A-D).<sup>56</sup> Then, we conducted immunofluorescence imaging to visualize the apoptosis in the cells treated with our molecules. We stained the cells for annexin-V (an apoptosis biomarker) and propidium iodide (PI, for tracking cell death) after treatment with our molecules (Figure 7E, F, S23, S24). We found a remarkable increase in the staining for annexin-V and PI in cells treated with our molecules, and a cotreatment with QVD-OPh rescued the PI staining (Figure 7E, F, S23, S24). Next, we performed immunoblotting for tracking the activation profiles of caspase cascade-mediated apoptosis markers. First, we confirmed the release of mitochondrial cytochrome-c (Cyt c) to the cytoplasm after treatment with our lead molecules and the positive control (Figure 7G). Then, a time-dependent (4 h and 8 h) analysis of full-length caspase-3 and its activation to release cleaved caspase-3 indicated a sharp increase in the caspase-3 activation over time and this was comparable to the positive control, staurosporine (Figure 7G, H, S25). The subsequent effect of caspase-3 activation to trigger the cleavage of death substrate, Poly [ADP-ribose] polymerase 1 (PARP-1) exhibited a strong correlation with our lead molecule-mediated apoptosis in two independent cell lines (Figure 7G, H, S25). Collectively, the above set of experiments strongly suggests that our lead molecules induce mitochondrial dysfunction and released Cyt c into the cytoplasm to trigger the caspase cascade that promoted the intrinsic apoptotic cell death mechanism in cancer cells.



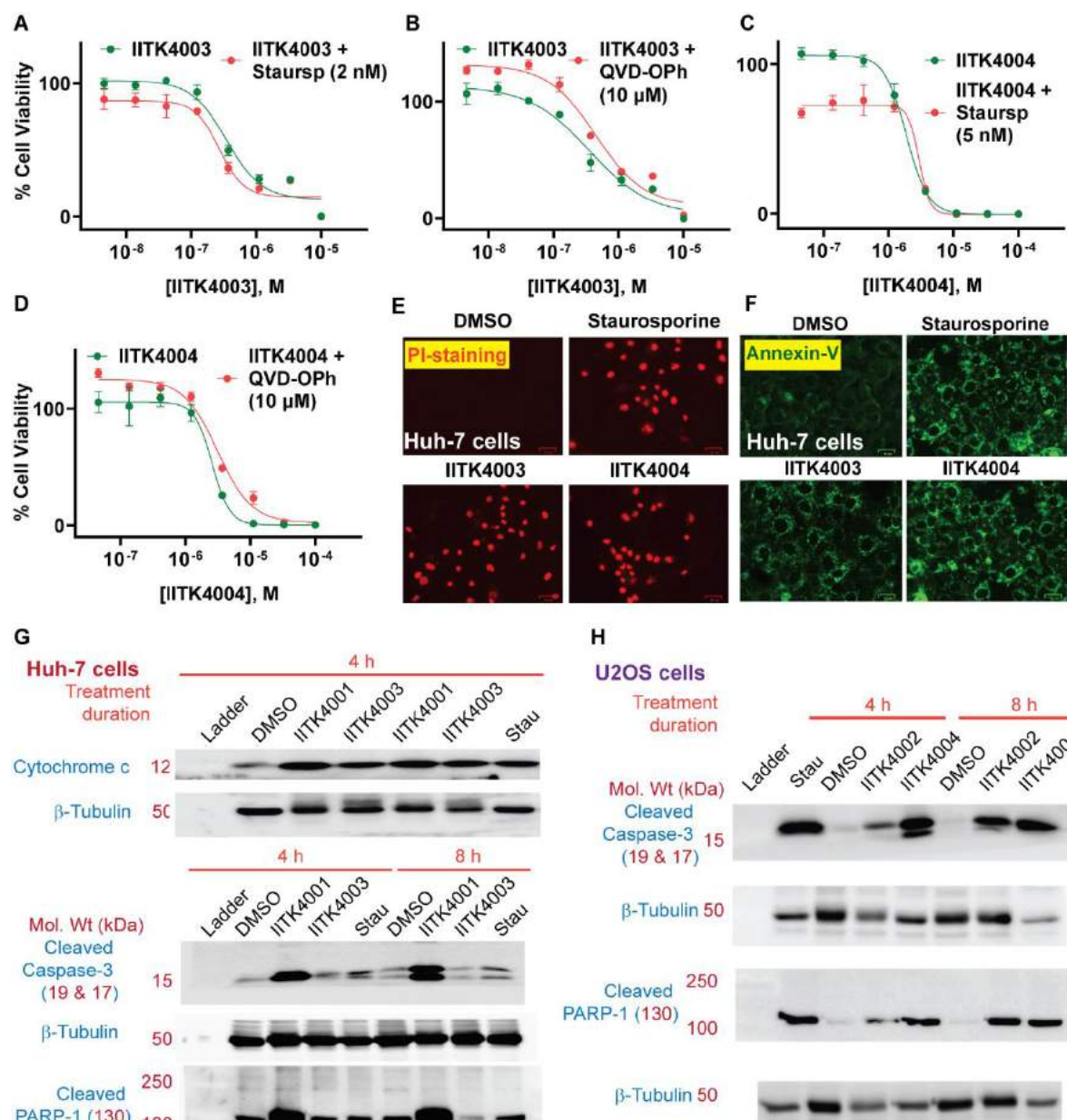


**Figure 7. IITK4003/ IITK4004 triggers the caspase cascade to promote apoptosis in cancer cells.**

(A-D) Cell viability studies of Huh-cells upon co-treatment of apoptosis inducer staurosporine (5 nM, A, C) and inhibitor QVD-OPh (10 μM, B, D) with our lead molecules.

(E, F) Induction of apoptosis in Huh-7 (E) and U2OS (F) cells by IITK4001/4003 (20 μM) and staurosporine (250 nM) was captured using a fluorescence imaging of propidium iodide (PI) stained nuclei and immunostaining for an apoptosis marker, Annexin-V.

(G, H) Immunoblotting for indicated apoptosis markers in Huh-7 (G) and U2OS cells (H) after 4 h and 8 h of treatment with IITK4001-IITK4004 (30 μM) and the positive control Staurosporine (100 nM). Protein concentration in each lane was 20 μg, all molecules were used at 30 μM, except Stau: Staurosporine, 100 nM). Graphs A-D indicate mean ± s.d. Data presented are performed in two independent cell lines and are representative of more than two independent experiments with a minimum of three technical replicates

### **Pan-cancer activity and 3D-spheroid growth inhibition by IITK4003/4004:**

Further, to emphasize the generality of IITK4003/IITK4004 to act as proliferation inhibitor of various cancer phenotypes, we have screened the indicated molecules against a panel of ten more cancer phenotypes in addition to Huh-7 and U2OS (Table 1, Figure S26). We observed

growth inhibition of cancer cells within a range of 0.3 - 3.5  $\mu\text{M}$   $\text{EC}_{50}$  against all the cancer lines investigated. We found Huh-7 cells to be highly sensitive to IITK4003 with an  $\text{EC}_{50}$  at 340 nM concentration, whereas other cancer phenotypes exhibited comparable sensitivity. Among the hepatocellular carcinoma (HCC) cells, the sensitivity of Huh-7 cells was nearly 10-fold higher than HepG2 cells (Table 1, Figure S26). These drastic differences in selectivity could be attributed to several factors including genetic and metabolic differences, and higher lipogenesis in Huh-7 cells over other hepatoma cells<sup>57-59</sup> which is an interesting lead for future explorations. In the case of IITK4004, the molecules exhibited comparable cell-killing potency (2.2 – 3.5  $\mu\text{M}$ ) with all the cancer cell lines tested (Table 1, Figure S26). Extending the studies to 3D-cell models such as spheroids will help us capture the ability of our molecules to penetrate the tissue-like structure and inhibit their growth. Therefore, we have generated 3D-spheroids of HepG2 cells and treated them with mitomycin as a positive control to establish the assay system is functional. Then the treatment of spheroids with IITK4003 and IITK4004, we found an excellent reduction in the scaffold size of spheroids in a dose-dependent fashion (Figure 8A-C). These results together highlight that these molecules can prevent multiple cancer phenotypes and they can be successful in inhibiting tumor growth in vivo as indicated by volume reduction in the prototype, 3D-spheroids.

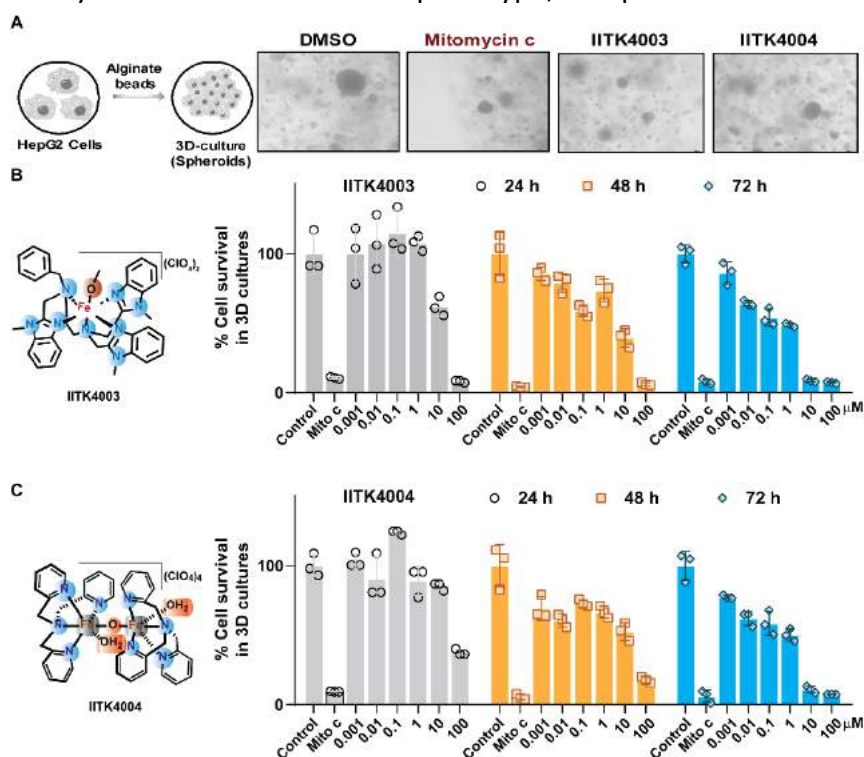


**Figure 8. Our lead molecules IITK4003/ IITK4004 reduced the 3D-spheroid volume and dose-dependently inhibited their growth.**

(A) Schematic and images of HepG2 cells spheroids generated out of 3D-culture and their treatment with indicated molecules after 72 h.

(B, C) 3D-culture cell viability was assessed during their treatment with IITK4003/IITK4004 for 24, 48, and 72 h using MTT assay.

Graphs b and c indicate mean  $\pm$  s.d. Data presented in a-c are representative of two or more independent experiments with a minimum of three technical replicates

**Table 1. Cell viability analysis of various cancer cell lines with IITK4003 and IITK4004**

Cancer Cell Line <sup>a</sup>	IITK4003, ( $\mu$ M)	IITK4004, ( $\mu$ M)
A549	1.99	2.3
HepG2	3.30	3.07
Jurkat-6	0.34	2.2
MCF7	1.60	2.2
MDA-MB-231	2.28	2.8
U2OS	2.10	2.9
A375	1.80	2.4
HCT116	N.d.	3.0
PC3	N.d.	3.5
RPMI 8226	N.d.	3.5
U87MG	N.d.	2.3

N.d. = Not determined. Cancer cell lines: A549: Lung carcinoma epithelial cells; HepG2 & Huh-7: Hepatocellular carcinoma; Jurkat J6: Acute T-cell Leukaemia; MCF7: Breast cancer MDA-MB-231; Triple negative breast cancer; U2OS: Osteosarcoma; A375: Melanoma; HCT-116: Colon cancer; PC3: Prostate cancer; RPMI 8226: B lymphocytes; U87MG: Glioblastoma.

#### **Nanocarrier potentiating the activity of IITK4003/4004 in liver cancer cells:**

Our studies for IITK4003 in multiple cancer phenotypes showed a variable  $EC_{50}$  (0.34 to 3.3  $\mu$ M, a 10-fold difference), whereas a comparable  $EC_{50}$  was recorded for IITK4004 (2.2 to 3.9  $\mu$ M) in all the cell lines investigated (Table 1, Figure S26). At higher concentrations we found aqueous solubility issues for IITK4003 over IITK4004, therefore it was suspected that the differential  $EC_{50}$  in various cell lines could be an outcome of differential solubility and cell permeability, as well. Hence, to evaluate this possibility and improve the local concentration intracellularly, a polymeric nanosized drug carrier was synthesized for the effective delivery of IITK4003 and IITK4004, which would overcome the problem associated with water solubility and cell permeability. A water-in-oil-in-water emulsion method (Scheme 3) was employed for the preparation of the nanocarriers (NCs) using an amphiphilic, diblock amphiphilic copolymer carboxylic acid poly (ethylene glycol)-block-poly(lactide-co-glycolide) (PLGA-b-PEG-COOH). The molecules of interest, IITK4003 and IITK4004, were added to the polymer solution at the first step of preparation of NCs which led to an effective entrapment of molecules, presumably inside the hydrophobic core of the nanocarriers (Scheme 4). Dynamic light scattering based investigation revealed that the effective hydrodynamic diameter of synthesized NCs was  $186 \pm 2.5$  nm. It was noticed that there was no significant change in effective hydrodynamic diameter of NCs on loading of the IITK4003 and IITK4004 in nanocarriers, called as NC/IITK4003 and NC/IITK4004, respectively (Figure 9A). The effective hydrodynamic diameter of NC/IITK4003 and NC/IITK4004 was  $184 \pm 1.5$  nm and  $183 \pm 7.5$  nm, respectively. The polydispersity index (PDI) values of NCs, NC/IITK4003 and NC/IITK4004 nanosuspension were found to be  $0.18 \pm 0.01$ ,  $0.14 \pm 0.01$  and  $0.23 \pm 0.02$ , respectively (Figure 9B). These low PDI values implied the homogeneous nature of the polymeric nanocarriers which was retained even after loading IITK4003 and IITK4004. This observation was also

supported by the intensity vs. size distribution plot as represented in Figure 8C for NCs and NC/IITK4003, NC/IITK4004 and their imaging (Figure 9D). Further, the loaded amount of IITK4003 and IITK4004 was quantified by analyzing the absorbance vs. concentration standard plot. It was found that the loaded concentration of IITK4003 and IITK4004 in NCs was 34.8 and 194  $\mu\text{M}$ , respectively (Figure 9E, F). This quantification deciphered that the entrapment of two water insoluble molecules, IITK4003 and IITK4004 inside polymeric NCs brought these molecules into aqueous suspension in significantly higher concentration and eventually be available to the biological system for uptake possibly through endocytosis.<sup>60-62</sup> These lead molecule-encapsulated nanocarriers were evaluated in both Huh-7 and HepG2 cells for their antiproliferative activity. NC/IITK4003 exhibited nearly a four-fold (0.43 to 0.11  $\mu\text{M}$ ) and twelve-fold (4.87 to 0.42  $\mu\text{M}$ ) enhancement in  $\text{EC}_{50}$  in Huh-7 and HepG2 cells, respectively (Figure 9G-K). Under comparable conditions, we found no significant difference in the  $\text{EC}_{50}$  for IITK4004 between the pristine treatment or nano-encapsulated form NC/IITK4004. Collectively, our effort to enhance the effective delivery of IITK4003 through nanoencapsulation resulted in the identification of exceptionally potent growth inhibition of Huh-7 cells at 110 nM  $\text{EC}_{50}$ .

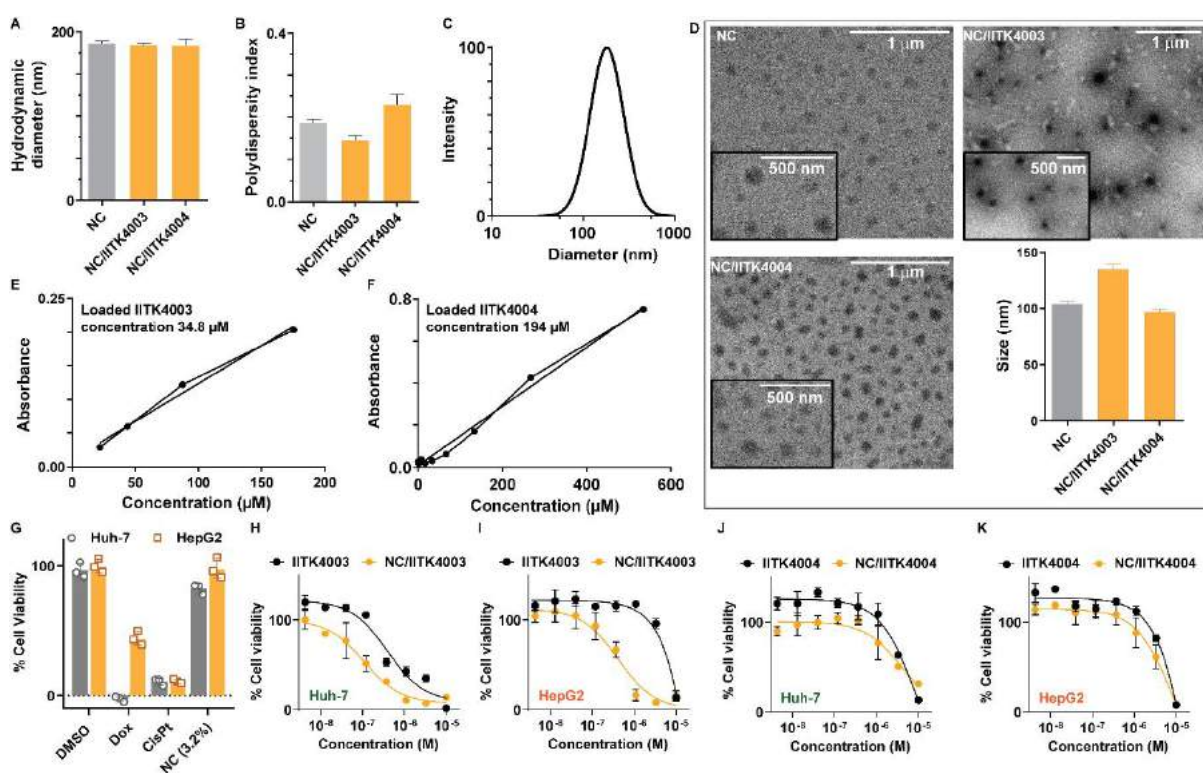


**Figure 9. Characterization of NCs, IITK4003 and IITK4004 loaded NCs and their antiproliferative activity studies**

(A) The hydrodynamic diameter of NCs, NC/ IITK4003 and NC/ IITK4004.

(B) Polydispersity index of NCs, NC/ IITK4003 and NC/ IITK4004.

(C) Representative intensity vs. diameter size distribution plot for NCs.

(D) Representative TEM image of NCs, NC/IITK4003 and NC/IITK4004. Anhydrous size of NCs, NC/IITK4003, and NC/IITK4004 samples as obtained from respective multiple TEM images.



(E, F) Representative absorbance vs. concentration standard plot for quantification of (E) IITK4003 loading and (F) IITK4004 loading.

(G-K) Cell viability studies of Huh-7 and U2OS cells upon treatment with IITK4003/4004, their nano-encapsulated forms and controls (G), IITK4003 and NC/IITK4003 (H, I), IITK4004 and NC/IITK4004 (J, K) in Huh-7 (data colored in gray) and U2OS (data colored in orange) cells.

Graphs A, B, D and G-K indicate mean  $\pm$  s.d. Data presented in G-K are representative of two or more independent experiments with a minimum of three technical replicates in each cell line.

## The impact of research on the advancements of cancer therapeutics

The emergence of multidrug resistance in cancer cells to existing drugs demands new therapeutics interventions. While organic molecules dominate the cancer therapeutics collections, evolution of biologics, antibody-drug conjugates and PROTACs are developing into unique modalities to target cancer. Among the metal-based drugs, cisplatin is an acclaimed cancer therapeutic, however, the development of new metal/metal-complex-based therapeutics are underdeveloped. We identified redox active iron complexes that exploited the weak link of mitochondrial redox sensitivity as an attractive mechanistic target. Our iron complexes induced oxidative stress and triggered intrinsic cancer cell apoptosis pathway at nanomolar doses, and a nanocarrier-mediated delivery further pronounced the antiproliferative effect in cancer cells. Together, iron complexes leveraging the mitochondrial redox sensitivity highlights a promising starting point towards developing next-generation cancer therapeutics.

## References

- 1) 1. Rosenberg, B., VanCamp, L., Trosko, J.E., and Mansour, V.H. (1969). Platinum compounds: a new class of potent antitumour agents. *Nature* 222, 385-386. 10.1038/222385a0.
- 2) 2. Jamieson, E.R., and Lippard, S.J. (1999). Structure, Recognition, and Processing of Cisplatin–DNA Adducts. *Chem. Rev.* 99, 2467-2498. 10.1021/cr980421n.
- 3) 3. Eskandari, A., Kundu, A., Ghosh, S., and Suntharalingam, K. (2019). A Triangular Platinum(II) Multinuclear Complex with Cytotoxicity Towards Breast Cancer Stem Cells. *Angew. Chem. Int. Ed.* 58, 12059-12064. <https://doi.org/10.1002/anie.201905389>.
- 4) 4. Jin, S., Muhammad, N., Sun, Y., Tan, Y., Yuan, H., Song, D., Guo, Z., and Wang, X. (2020). Multispecific Platinum(IV) Complex Deters Breast Cancer via Interposing Inflammation and Immunosuppression as an Inhibitor of COX-2 and PD-L1. *Angew. Chem. Int. Ed.* 59, 23313-23321. <https://doi.org/10.1002/anie.202011273>.
- 5) 5. Laws, K., Bineva-Todd, G., Eskandari, A., Lu, C., O'Reilly, N., and Suntharalingam, K. (2018). A Copper(II) Phenanthroline Metallopeptide That Targets and Disrupts Mitochondrial Function in Breast Cancer Stem Cells. *Angew. Chem. Int. Ed.* 57, 287-291. 10.1002/anie.201710910.
- 6) 6. Xiao, Z., Johnson, A., Singh, K., and Suntharalingam, K. (2021). The Discrete Breast Cancer Stem Cell Mammosphere Activity of Group 10-Bis(azadiphosphine) Metal Complexes. *Angew. Chem. Int. Ed.* 60, 6704-6709. <https://doi.org/10.1002/anie.202014242>.
- 7) 7. Clarke, M.J., Zhu, F., and Frasca, D.R. (1999). Non-Platinum Chemotherapeutic Metallopharmaceuticals. *Chem. Rev.* 99, 2511-2534. 10.1021/cr9804238.
- 8) 8. Eskandari, A., and Suntharalingam, K. (2019). A reactive oxygen species-generating, cancer stem cell-potent manganese(ii) complex and its encapsulation into polymeric nanoparticles. *Chem. Sci.* 10, 7792-7800. 10.1039/C9SC01275C.

- 9) 9. Suntharalingam, K., Lin, W., Johnstone, T.C., Bruno, P.M., Zheng, Y.-R., Hemann, M.T., and Lippard, S.J. (2014). A Breast Cancer Stem Cell-Selective, Mammospheres-Potent Osmium(VI) Nitrido Complex. *J. Am. Chem. Soc.* **136**, 14413-14416. 10.1021/ja508808v.
- 10) 10. Gill, M.R., Cecchin, D., Walker, M.G., Mulla, R.S., Battaglia, G., Smythe, C., and Thomas, J.A. (2013). Targeting the endoplasmic reticulum with a membrane-interactive luminescent ruthenium(II) polypyridyl complex†Electronic supplementary information (ESI) available: Experimental details, characterization of 2 and Fig. S1-S6. See DOI: 10.1039/c3sc51725jClick here for additional data file. *Chem. Sci.* **4**, 4512-4519. 10.1039/c3sc51725j.
- 11) 11. Clavel, C.M., Păunescu, E., Nowak-Sliwiska, P., Griffioen, A.W., Scopelliti, R., and Dyson, P.J. (2015). Modulating the Anticancer Activity of Ruthenium(II)-Arene Complexes. *J. Med. Chem.* **58**, 3356-3365. 10.1021/jm501655t.
- 12) 12. Pettinari, R., Pettinari, C., Marchetti, F., Skelton, B.W., White, A.H., Bonfili, L., Cuccioloni, M., Mozzicafreddo, M., Cecarini, V., Angeletti, M., et al. (2014). Arene-ruthenium(II) acylpyrazolonato complexes: apoptosis-promoting effects on human cancer cells. *J. Med. Chem.* **57**, 4532-4542. 10.1021/jm500458c.
- 13) 13. Hentze, M.W., Muckenthaler, M.U., Galy, B., and Camaschella, C. (2010). Two to Tango: Regulation of Mammalian Iron Metabolism. *Cell* **142**, 24-38. <https://doi.org/10.1016/j.cell.2010.06.028>.
- 14) 14. Bogdan, A.R., Miyazawa, M., Hashimoto, K., and Tsuji, Y. (2016). Regulators of Iron Homeostasis: New Players in Metabolism, Cell Death, and Disease. *Trends Biochem. Sci.* **41**, 274-286. <https://doi.org/10.1016/j.tibs.2015.11.012>.
- 15) 15. Zhang, Y., He, J., Jin, J., and Ren, C. (2022). Recent advances in the application of metallomics in diagnosis and prognosis of human cancer. *Metallomics* **14**, mfac037. 10.1093/mtomcs/mfac037.
- 16) 16. Abedi, M., and Rahgozar, S. (2022). Puzzling out iron complications in cancer drug resistance. *Crit. Rev. Oncol. Hematol.* **178**, 103772 (103771-103719). <https://doi.org/10.1016/j.critrevonc.2022.103772>.
- 17) 17. Andrews, N.C. (2000). Iron homeostasis: insights from genetics and animal models. *Nat. Rev. Genet.* **1**, 208-217. 10.1038/35042073.
- 18) 18. Shen, Y., Zhang, B., Su, Y., Badshah, S.A., Wang, X., Li, X., Xue, Y., Xie, L., Wang, Z., Yang, Z., et al. (2020). Iron Promotes Dihydroartemisinin Cytotoxicity via ROS Production and Blockade of Autophagic Flux via Lysosomal Damage in Osteosarcoma. *Front. Pharmacol.* **11**. 10.3389/fphar.2020.00444.
- 19) 19. Raza, M., Chakraborty, S., Choudhury, M., Ghosh, C.P., and Nag, A. (2014). Cellular Iron Homeostasis and Therapeutic Implications of Iron Chelators in Cancer. *Curr. Pharm. Biotechnol.* **15**, 1125-1140. <http://dx.doi.org/10.2174/138920101512141202111915>.
- 20) 20. Kew, M.C. (2009). Hepatic iron overload and hepatocellular carcinoma. *Cancer Lett.* **286**, 38-43. 10.1016/j.canlet.2008.11.001.
- 21) 21. Tsvetkov, P., Coy, S., Petrova, B., Dreishpoon, M., Verma, A., Abdusamad, M., Rossen, J., Joesch-Cohen, L., Humeidi, R., Spangler, R.D., et al. (2022). Copper induces cell death by targeting lipoylated TCA cycle proteins. *Science (New York, N.Y.)* **375**, 1254-1261. doi:10.1126/science.abf0529.
- 22) 22. Cui, L., Gouw, A.M., LaGory, E.L., Guo, S., Attarwala, N., Tang, Y., Qi, J., Chen, Y.-S., Gao, Z., Casey, K.M., et al. (2021). Mitochondrial copper depletion suppresses triple-negative breast cancer in mice. *Nat. Biotechnol.* **39**, 357-367. 10.1038/s41587-020-0707-9.
- 23) 23. Ramchandani, D., Berisa, M., Tavarez, D.A., Li, Z., Miele, M., Bai, Y., Lee, S.B., Ban, Y., Dephore, N., Hendrickson, R.C., et al. (2021). Copper depletion modulates mitochondrial oxidative phosphorylation to impair triple negative breast cancer metastasis. *Nat. Commun.* **12**, 7311. 10.1038/s41467-021-27559-z.
- 24) 24. Warburg, O., Wind, F., and Negelein, E. (1927). The metabolism of tumours in the body. *J. Gen. Physiol.* **8**, 519-530. 10.1085/jgp.8.6.519.

- 25) 25. Bravin, C., Badetti, E., Licini, G., and Zonta, C. (2021). Tris(2-pyridylmethyl)amines as emerging scaffold in supramolecular chemistry. *Coord. Chem. Rev.* **427**, 213558 (213551-213519). <https://doi.org/10.1016/j.ccr.2020.213558>.
- 26) 26. Hentze, M.W., Muckenthaler, M.U., and Andrews, N.C. (2004). Balancing acts: molecular control of mammalian iron metabolism. *Cell* **117**, 285-297. 10.1016/s0092-8674(04)00343-5.
- 27) 27. Liu, J., Chakraborty, S., Hosseinzadeh, P., Yu, Y., Tian, S., Petrik, I., Bhagi, A., and Lu, Y. (2014). Metalloproteins Containing Cytochrome, Iron–Sulfur, or Copper Redox Centers. *Chem. Rev.* **114**, 4366-4469. 10.1021/cr400479b.
- 28) 28. Papanikolaou, G., and Pantopoulos, K. (2005). Iron metabolism and toxicity. *Toxicol. Appl. Pharmacol.* **202**, 199-211. 10.1016/j.taap.2004.06.021.
- 29) 29. Nagao, H., Komeda, N., Mukaida, M., Suzuki, M., and Tanaka, K. (1996). Structural and Electrochemical Comparison of Copper(II) Complexes with Tripodal Ligands. *Inorg. Chem.* **35**, 6809-6815. 10.1021/ic960303n.
- 30) 30. Nanthakumar, A., Fox, S., Murthy, N.N., and Karlin, K.D. (1997). Inferences from the <sup>1</sup>H-NMR Spectroscopic Study of an Antiferromagnetically Coupled Heterobinuclear Fe(III)–(X)–Cu(II) S = 2 Spin System (X = O<sub>2</sub><sup>-</sup>, OH<sup>-</sup>). *J. Am. Chem. Soc.* **119**, 3898-3906. 10.1021/ja962404q.
- 31) 31. Szajna, E., Dobrowolski, P., Fuller, A.L., Arif, A.M., and Berreau, L.M. (2004). NMR Studies of Mononuclear Octahedral Ni(II) Complexes Supported by Tris((2-pyridyl)methyl)amine-Type Ligands. *Inorg. Chem.* **43**, 3988-3997. 10.1021/ic040002a.
- 32) 32. Dharmaraja, A.T. (2017). Role of Reactive Oxygen Species (ROS) in Therapeutics and Drug Resistance in Cancer and Bacteria. *J. Med. Chem.* **60**, 3221-3240. 10.1021/acs.jmedchem.6b01243.
- 33) 33. Dickinson, B.C., and Chang, C.J. (2011). Chemistry and biology of reactive oxygen species in signaling or stress responses. *Nat. Chem. Biol.* **7**, 504-511. 10.1038/nchembio.607.
- 34) 34. D'Autréaux, B., and Toledano, M.B. (2007). ROS as signalling molecules: mechanisms that generate specificity in ROS homeostasis. *Nat. Rev. Mol. Cell Biol.* **8**, 813-824. 10.1038/nrm2256.
- 35) 35. Kim, C., Chen, K., Kim, J., and Que, L. (1997). Stereospecific Alkane Hydroxylation with H<sub>2</sub>O<sub>2</sub> Catalyzed by an Iron(II)–Tris(2-pyridylmethyl)amine Complex. *J. Am. Chem. Soc.* **119**, 5964-5965. 10.1021/ja9642572.
- 36) 36. Kim, H., Esser, L., Hossain, M.B., Xia, D., Yu, C.-A., Rizo, J., van der Helm, D., and Deisenhofer, J. (1999). Structure of Antimycin A1, a Specific Electron Transfer Inhibitor of Ubiquinol–Cytochrome c Oxidoreductase. *J. Am. Chem. Soc.* **121**, 4902-4903. 10.1021/ja990190h.
- 37) 37. Chen, K., Costas, M., Kim, J., Tipton, A.K., and Que, L. (2002). Olefin Cis-Dihydroxylation versus Epoxidation by Non-Heme Iron Catalysts: Two Faces of an Fe(III)–OOH Coin. *J. Am. Chem. Soc.* **124**, 3026-3035. 10.1021/ja0120025.
- 38) 38. Ho, R.Y.N., Roelfes, G., Feringa, B.L., and Que, L. (1999). Raman Evidence for a Weakened O–O Bond in Mononuclear Low-Spin Iron(III)–Hydroperoxides. *J. Am. Chem. Soc.* **121**, 264-265. 10.1021/ja982812p.
- 39) 39. Lim, M.H., Rohde, J.-U., Stubna, A., Bukowski, M.R., Costas, M., Ho, R.Y.N., Münck, E., Nam, W., and Que, L. (2003). An Fe<sup>IV</sup>O complex of a tetradentate tripodal nonheme ligand. *Proc. Natl. Acad. Sci. U.S.A.* **100**, 3665-3670. doi:10.1073/pnas.0636830100.
- 40) 40. Kim, J., Larka, E., Wilkinson, E.C., and Que Jr, L. (1995). An Alkylperoxoiron(III) Intermediate and Its Role in the Oxidation of Aliphatic C–H Bonds. *Angew. Chem. Int. Ed.* **34**, 2048-2051. <https://doi.org/10.1002/anie.199520481>.
- 41) 41. Mairata i Payeras, A., Ho, R.Y.N., Fujita, M., and Que, J.L. (2004). The Reaction of [Fe(II)(tpa)] with H<sub>2</sub>O<sub>2</sub> in Acetonitrile and Acetone—Distinct Intermediates and Yet Similar Catalysis. *Chem. Eur. J.* **10**, 4944-4953. <https://doi.org/10.1002/chem.200400480>.

- 42) 42. Dharmaraja, A.T., and Chakrapani, H. (2014). A Small Molecule for Controlled Generation of Reactive Oxygen Species (ROS). *Org. Lett.* 16, 398-401. 10.1021/ol403300a.
- 43) 43. Zielonka, J., Vasquez-Vivar, J., and Kalyanaraman, B. (2008). Detection of 2-hydroxyethidium in cellular systems: a unique marker product of superoxide and hydroethidine. *Nat. Protoc.* 3, 8-21. 10.1038/nprot.2007.473.
- 44) 44. Kelkar, D.S., Ravikumar, G., Mehendale, N., Singh, S., Joshi, A., Sharma, A.K., Mhetre, A., Rajendran, A., Chakrapani, H., and Kamat, S.S. (2019). A chemical–genetic screen identifies ABHD12 as an oxidized-phosphatidylserine lipase. *Nat. Chem. Biol.* 15, 169-178. 10.1038/s41589-018-0195-0.
- 45) 45. Garcia-Irigoyen, O., Bovenga, F., Piglionica, M., Piccinin, E., Cariello, M., Arconzo, M., Peres, C., Corsetto, P.A., Rizzo, A.M., Ballanti, M., et al. (2022). Enterocyte superoxide dismutase 2 deletion drives obesity. *iScience* 25, 103707. 10.1016/j.isci.2021.103707.
- 46) 46. Pannu, V., Rida, P.C.G., Ogden, A., Clewley, R., Cheng, A., Karna, P., Lopus, M., Mishra, R.C., Zhou, J., and Aneja, R. (2012). Induction of robust de novo centrosome amplification, high-grade spindle multipolarity and metaphase catastrophe: a novel chemotherapeutic approach. *Cell Death Dis.* 3, e346-e346. 10.1038/cddis.2012.82.
- 47) 47. Dixon, Scott J., Lemberg, Kathryn M., Lamprecht, Michael R., Skouta, R., Zaitsev, Eleina M., Gleason, Caroline E., Patel, Darpan N., Bauer, Andras J., Cantley, Alexandra M., Yang, Wan S., et al. (2012). Ferroptosis: An Iron-Dependent Form of Nonapoptotic Cell Death. *Cell* 149, 1060-1072. <https://doi.org/10.1016/j.cell.2012.03.042>.
- 48) 48. Palmer, G., Horgan, D.J., Tisdale, H., Singer, T.P., and Beinert, H. (1968). Studies on the respiratory chain-linked reduced nicotinamide adenine dinucleotide dehydrogenase. XIV. Location of the sites of inhibition of rotenone, barbiturates, and piericidin by means of electron paramagnetic resonance spectroscopy. *J. Biol. Chem.* 243, 844-847.
- 49) 49. Alexandre, A., and Lehninger, A.L. (1984). Bypasses of the antimycin a block of mitochondrial electron transport in relation to ubiquinone function. *Biochim. Biophys. Acta.* 767, 120-129. 10.1016/0005-2728(84)90086-0.
- 50) 50. Yoshikawa, S., Shinzawa-Itoh, K., Nakashima, R., Yaono, R., Yamashita, E., Inoue, N., Yao, M., Fei, M.J., Libeu, C.P., Mizushima, T., et al. (1998). Redox-Coupled Crystal Structural Changes in Bovine Heart Cytochrome c Oxidase. *Science (New York, N.Y.)* 280, 1723-1729. doi:10.1126/science.280.5370.1723.
- 51) 51. Green, D.R., and Reed, J.C. (1998). Mitochondria and Apoptosis. *Science (New York, N.Y.)* 281, 1309-1312. doi:10.1126/science.281.5381.1309.
- 52) 52. Liu, X., Kim, C.N., Yang, J., Jemmerson, R., and Wang, X. (1996). Induction of apoptotic program in cell-free extracts: requirement for dATP and cytochrome c. *Cell* 86, 147-157. 10.1016/s0092-8674(00)80085-9.
- 53) 53. Wang, C., and Youle, R.J. (2009). The role of mitochondria in apoptosis\*. *Annu. Rev. Genet.* 43, 95-118. 10.1146/annurev-genet-102108-134850.
- 54) 54. Wang, Y., Wang, M., Djekidel, M.N., Chen, H., Liu, D., Alt, F.W., and Zhang, Y. (2021). eccDNAs are apoptotic products with high innate immunostimulatory activity. *Nature* 599, 308-314. 10.1038/s41586-021-04009-w.
- 55) 55. Belmokhtar, C.A., Hillion, J., and Ségal-Bendirdjian, E. (2001). Staurosporine induces apoptosis through both caspase-dependent and caspase-independent mechanisms. *Oncogene* 20, 3354-3362. 10.1038/sj.onc.1204436.
- 56) 56. Caserta, T.M., Smith, A.N., Gultice, A.D., Reedy, M.A., and Brown, T.L. (2003). Q-VD-OPh, a broad spectrum caspase inhibitor with potent antiapoptotic properties. *Apoptosis : an international journal on programmed cell death* 8, 345-352. 10.1023/a:1024116916932.
- 57) 57. Nwosu, Z.C., Battello, N., Rothley, M., Piorońska, W., Sitek, B., Ebert, M.P., Hofmann, U., Sleeman, J., Wölfl, S., Meyer, C., et al. (2018). Liver cancer cell lines distinctly mimic the metabolic gene expression pattern of the corresponding human tumours. *J. Exp. Clin. Cancer Res.* 37, 211. 10.1186/s13046-018-0872-6.



- 58) 58. Shi, J., Wang, X., Lyu, L., Jiang, H., and Zhu, H.-J. (2018). Comparison of protein expression between human livers and the hepatic cell lines HepG2, Hep3B, and Huh7 using SWATH and MRM-HR proteomics: Focusing on drug-metabolizing enzymes. *Drug Metab. Pharmacokinet.* 33, 133-140. <https://doi.org/10.1016/j.dmpk.2018.03.003>.
- 59) 59. Gunn, P.J., Green, C.J., Pramfalk, C., and Hodson, L. (2017). In vitro cellular models of human hepatic fatty acid metabolism: differences between Huh7 and HepG2 cell lines in human and fetal bovine culturing serum. *Physiol. Rep.* 5, e13532. <https://doi.org/10.14814/phy2.13532>.
- 60) 60. Raza, K., Kumar, N., Misra, C., Kaushik, L., Guru, S.K., Kumar, P., Malik, R., Bhushan, S., and Katare, O.P. (2016). Dextran-PLGA-loaded docetaxel micelles with enhanced cytotoxicity and better pharmacokinetic profile. *Int. J. Biol. Macromol.* 88, 206-212. 10.1016/j.ijbiomac.2016.03.064.
- 61) 61. Xu, Z., Zhu, S., Wang, M., Li, Y., Shi, P., and Huang, X. (2015). Delivery of Paclitaxel Using PEGylated Graphene Oxide as a Nanocarrier. *ACS Appl. Mater. Interfaces* 7, 1355-1363. 10.1021/am507798d.
- 62) 62. Misra, S.K., Wu, Z., Ostadhossein, F., Ye, M., Boateng, K., Schulten, K., Tajkhorshid, E., and Pan, D. (2019). Pro-Nifuroxazide Self-Assembly Leads to Triggerable Nanomedicine for Anti-cancer Therapy. *ACS Appl. Mater. Interfaces* 11, 18074-18089. 10.1021/acsami.9b01343.
- 63) 63. Vacca, A., Bruno, M., Boccarelli, A., Coluccia, M., Ribatti, D., Bergamo, A., Garbisa, S., Sartor, L., and Sava, G. (2002). Inhibition of endothelial cell functions and of angiogenesis by the metastasis inhibitor NAMI-A. *Br. J. Cancer* 86, 993-998. 10.1038/sj.bjc.6600176.
- 64) 64. Frausin, F., Scarcia, V., Cocchietto, M., Furlani, A., Serli, B., Alessio, E., and Sava, G. (2005). Free Exchange across Cells, and Echinatin-Sensitive Membrane Target for the Metastasis Inhibitor NAMI-A (Imidazolium  $\alpha$ -Imidazole Dimethyl Sulfoxide Tetrachlororuthenate) on KB Tumor Cells. *J. Pharmacol. Exp. Ther.* 313, 227-233. 10.1124/jpet.104.078352.
- 65) 65. Sava, G., Frausin, F., Cocchietto, M., Vita, F., Podda, E., Spessotto, P., Furlani, A., Scarcia, V., and Zabucchi, G. (2004). Actin-dependent tumour cell adhesion after short-term exposure to the antimetastasis ruthenium complex NAMI-A. *Eur. J. Cancer* 40, 1383-1396. <https://doi.org/10.1016/j.ejca.2004.01.034>.
- 66) 66. Garzon, F.T., Berger, M.R., Keppler, B.K., and Schmähl, D. (1987). Comparative antitumor activity of ruthenium derivatives with 5'-deoxy-5-fluorouridine in chemically induced colorectal tumors in SD rats. *Cancer Chemother. Pharmacol.* 19, 347-349. 10.1007/BF00261487.
- 67) 67. Keppler, B.K., and Rupp, W. (1986). Antitumor activity of imidazolium-bisimidazole-tetrachlororuthenate (III). *J. Cancer Res. Clin. Oncol.* 111, 166-168. 10.1007/BF00400758.
- 68) 68. Romero-Canelón, I., and Sadler, P.J. (2013). Next-Generation Metal Anticancer Complexes: Multitargeting via Redox Modulation. *Inorg. Chem.* 52, 12276-12291. 10.1021/ic400835n.
- 69) 69. Yellol, J., Pérez, S.A., Buceta, A., Yellol, G., Donaire, A., Szumlas, P., Bednarski, P.J., Makhouloufi, G., Janiak, C., Espinosa, A., and Ruiz, J. (2015). Novel C,N-Cyclometalated Benzimidazole Ruthenium(II) and Iridium(III) Complexes as Antitumor and Antiangiogenic Agents: A Structure-Activity Relationship Study. *J. Med. Chem.* 58, 7310-7327. 10.1021/acs.jmedchem.5b01194.
- 70) 70. Gill, M.R., Harun, S.N., Halder, S., Boghazian, R.A., Ramadan, K., Ahmad, H., and Vallis, K.A. (2016). A ruthenium polypyridyl intercalator stalls DNA replication forks, radiosensitizes human cancer cells and is enhanced by Chk1 inhibition. *Sci. Rep.* 6, 31973-31973. 10.1038/srep31973.
- 71) 71. Zeng, L., Gupta, P., Chen, Y., Wang, E., Ji, L., Chao, H., and Chen, Z.-S. (2017). The development of anticancer ruthenium(II) complexes: from single molecule compounds to nanomaterials. *Chem. Soc. rev.* 46, 5771-5804. 10.1039/c7cs00195a.

- 72) 72. Lin, Y., Choksi, S., Shen, H.M., Yang, Q.F., Hur, G.M., Kim, Y.S., Tran, J.H., Nedospasov, S.A., and Liu, Z.G. (2004). Tumor necrosis factor-induced nonapoptotic cell death requires receptor-interacting protein-mediated cellular reactive oxygen species accumulation. *J. Biol. Chem.* 279, 10822-10828. 10.1074/jbc.M313141200.
- 73) 73. Weinlich, R., Oberst, A., Beere, H.M., and Green, D.R. (2017). Necroptosis in development, inflammation and disease. *Nat. Rev. Mol. Cell Biol.* 18, 127-136. 10.1038/nrm.2016.149.

V. Sai Kumar